Spring 1-1-2018

In-Situ Measurements of the Elastic Modulus of Zirconia Polycrystals Held in a State of Flash Induced by an Electric Field

Rushi Keshav Kathiria
University of Colorado at Boulder, rushi.kathiria@colorado.edu

In-Situ Measurements of the Elastic Modulus of zirconia polycrystals held in a state of Flash Induced by an Electric Field

by

Rushi Keshav Kathiria

B.E., K.J. Somaiya College of Engineering, India, 2016

A thesis submitted to the

Faculty of the Graduate School of the

University of Colorado in partial fulfillment

of the requirements for the degree of

Master of Science

Department of Mechanical Engineering

2018

This thesis entitled:
In-Situ Measurements of the Elastic Modulus of zirconia polycrystals held in a state of Flash Induced by an Electric Field
written by Rushi Keshav Kathiria
has been approved for the Department of Mechanical Engineering

_____
Prof. Rishi Raj

_____
Prof. Todd Murray

_____
Prof. Mahamoud I. Hussein

Date _____

The final copy of this thesis has been examined by the signatories, and we find that both the content and the form meet acceptable presentation standards of scholarly work in the above mentioned discipline.

Kathiria, Rushi Keshav (M.S., Mechanical Engineering)

In-Situ Measurements of the Elastic Modulus of zirconia polycrystals held in a state of Flash Induced by an Electric Field

Thesis directed by Prof. Rishi Raj

A recently discovered sintering mechanism called flash sintering where densification of a green ceramic compact happens in seconds rather than hours is the interest of this work. A rather interesting result is found at the end of this work about the effect of flash on the elastic modulus of 3mol% Yttria-Partially stabilized zirconia (3Y-TZP) during flash. To interpret the relation between natural frequency and elastic modulus of a cantilever beam,Euler-Bernoulli beam theory coupled with a spring mass damper system was used. Fast Fourier Transform and Finite Element Analysis were employed to analyze the material vibrations and measure the change in natural frequency and elastic modulus of softened region. Initial experiments were performed in a furnace to get a baseline plot of elastic modulus vs temperature (up to $1200°C$), which is an inverted 'S' shape curve stabilizing at higher temperatures. Also, measurements were conducted while maintaining flash for four current densities: 60, 80, 100, and $120\ mA\ mm^{-2}$ covering a range of flash lengths (10, 20, and $30\ mm$) and furnace off state. Damping coefficient was also calculated simultaneously to obtain the undamped natural frequency. This work confirms the supposition that there is softening of elastic modulus with the effect becoming more prominent with increasing current densities when in the state of flash. A drop of 30% in elastic modulus has been observed during flash with respect to the modulus at that temperature (without flash).

Acknowledgements

This research was supported by the Department of Energy.

This thesis would not have been possible without Professor Rishi Raj, whose guidance, support, and mentorship is highly treasured. Also, special thanks to Professor Mahmoud I. Hussein and the Aerospace department at University of Colorado Boulder for providing the equipment, without which this thesis would be impossible.

Special thanks to everyone in Raj lab namely: Dr. Devinder Yadav, Dr. Rubens Ingraci, Dr. Punith Gowda, Bola Yoon, Viviana Avila, Thomas Clemenceau, Niriaina Andriamady, SeoHyeon Jo, and Mark Spowart for helping me with my research.

Finally, I am grateful to my family and friends for their unending love, support, and patience.

Contents

Chapter

Tables

Table

Figures

Figure

Chapter 1

Introduction

Pottery among various other artifacts has been an integral part of human civilization for centuries. Some of its uses being: storage, cooling liquids, decorative set pieces. This pottery is nothing but when wet clay is molded into different shapes for various reasons. Only when heated and dried, this clay turns into something hard, strong and usable. This process of heating an unfinished product for hardening is called sintering.

This past century has seen an immense growth of this process on different kinds of materials for forging a variety of products. Over the past few decades, sintering has primarily been used in the ceramic industry which has seen a five fold increase in turn over along with considerable number of publications. [1]

Easy availability and abundance of raw material coupled with desirable mechanical, optical and electrical properties has led to a widespread use of ceramic products in most industrial sectors. Ceramics in particular offer wide variety of properties such as high elastic modulus, high thermal resistance, varying optical properties, piezoelectricity, etc. for large applications in the field of tiles, semiconductors, optical devices, high temperature turbine blades, etc.

Sintering of a ceramic material is only possible at very high temperatures to obtain highly dense products from green powder compacts. Densification in case of ceramics is a result of

continuous solid state mass transport of particles to reduce the excess surface energy at the beginning. Several different techniques used for sintering are discussed in upcoming sections. However, the main focus of this thesis is the recently discovered flash sintering technique, where densification is achieved in seconds instead of minutes and hours without any loss in mechanical properties. Not much is known about the underlying mechanism and about the behavior of materials during flash.

The commercial applications of flash sintering could be immense once it is fully understood. Yang and Conrad [2] reported an increase in strain rate and elongation under the application of very high electric fields and low currents. This idea of increased plasticity perceives the notion of reduced elastic modulus. Lower elastic modulus means reduced strain energy which in turn reduces the activation energy barrier for particle movement promoting a higher generation of defects (Frenkels in particular). Hence, measuring the effect of flash (electric field) on the elastic modulus of the material was the primary objective of this thesis. A cantilever beam combined with its finite element simulations was used to estimate these changes by measuring the changes in natural (first harmonic) frequency. These results then were used to predict the possible effect for flash.

Chapter 2

Literature Review

The topics covered in this chapter are the basis of this thesis. It reviews the sintering process (specifically solid-state diffusion mechanism) in ceramics, its thermodynamics, different stages of sintering, and different types of sintering techniques with an emphasis on field-assisted and flash sintering. Additionally, this chapter covers the vibration of cantilever beams using the Euler-Bernoulli beam theory and its relation to natural (fundamental) frequency, elastic modulus, and damping coefficient of the beam.

2.1 Sintering

Sintering is an irreversible thermodynamic process where green powder compacts are heated to specified temperatures causing densification of the compact. The basic phenomena occurring in sintering are densification and grain growth. This densification is a result of mass transport at the atomic scale in order to reduce the interfacial energy [1]. Sintering, in general, is used to manufacture powdered metallurgical parts and ceramic components, however, the techniques employed may be different depending on the material, powder and final properties required.

Although the techniques employed may be different, the steps involved are same. The process begins by making a slurry of powder and binder in certain proportion for easy handling. Green bodies are then formed by applying pressure. Sintering processes can be divided into two main types: solid state sintering and liquid phase sintering. Liquid phase is further divided into

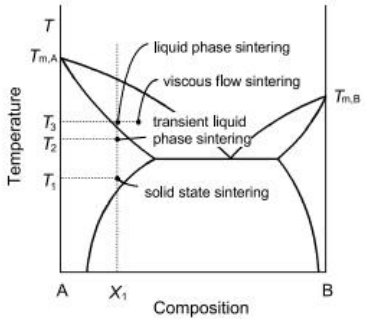

Figure 2.1: Illustration of various types of sintering [3]

transient liquid phase and viscous flow sintering as can be seen in Figure 2.1. Solid state sintering occurs completely in solid state where as liquid phase sintering occurs in a liquid or viscous phase depending on the temperature. This thesis deals with the sintering of 3YSZ (ceramic powder) which involves solid state mass transport instead of liquid and viscous phase.

The driving force behind this process is the total excess interfacial energy. This excess surface energy of a green body is expressed as a product of specific surface energy and surface area. Pores present in the compact largely contribute to large interfacial energy. Filling up these pores by particles reduces the surface area resulting in lower energy system. This densification and grain growth is affected by a number of variables called the sintering variables. Sintering variables are of two types: material and process. Material variables consist of powder size, shape, chemical composition, etc whereas process variables include thermodynamic variables such as temperature, atmosphere, pressure, time, etc. [3]

2.1.1 Thermodynamics of Sintering

Densification and grain growth are related to temperature of sintering; Higher the temperature, greater is the energy of atoms and hence, higher sintering rate. Temperature aside, surface energy is the main thermodynamic cause of sintering. Sintering is the result of reduction in interfacial energy which inturn leads to densification and grain growth. Here, surface is

a plane separating different matters, particles, pores and phases. These surfaces are the reason for excess interfacial energy which consumed by particles from the bulk of the system. Since, powders with smaller particle size have greater surface area and energy (assuming particle to be spherical) making it easier for them to diffuse through when compared to bigger sized particles. Hence, powders with small particle size have a higher sintering rate.

In an ideal crystal lattice, every atom is surrounded by corresponding atoms (no free surface) and hence is energetically stable. But, when one or a few atomic bonds are broken (free surface), the atom is no longer stable due to the available excess energy from broken bonds corresponding to the surface energy. This difference in energy between the excess surface and bulk energy creates a potential/stress that leads to in mass transport. This stress is called the sintering stress. An empirical relation for sintering stress is derived from the thermodynamic potential of surface and is a product of the specific surface energy and curvature as seen in equation 2.1.

$$\sigma = \gamma(\frac{1}{R_1} + \frac{1}{R_2}) \tag{2.1}$$

Here, γ is the specific surface energy, and R_1 and R_2 are the radii of curvature for the surface. Usually surface energy for solids is around $1\ J/m^2$ [4]. Since the mass transports at these curved interfaces, eventually the curvature reduces make it more flatter. Hence the sintering stress drops slowing down mass transport until an equilibrium is achieved. Mass transport or movement of atoms is only possible if these atoms can break free from its neighbors and have enough energy to diffuse. This energy is stimulated in the form of heat to create vacancies and active atoms. Atomic motion is more likely to happen if there is a near by vacant site. This probability of atoms having enough energy is described by an Arrhenius relation as shown in equation 2.2 where, Q is the activation energy, R the gas constant, N_0 number of vacancies, N_A is the number of active atoms, and T the temperature for sintering. Here, the activation energy Q is the sum of vacancy formation energy and energy required to break bonds [5]. Therefore, higher temperatures results

in a high number of active atoms implying faster sintering rate.

$$N_A = N_0 exp\left(-\frac{Q}{RT}\right) \tag{2.2}$$

2.1.2 Mechanisms of Sintering

Sintering mechanisms, in general, are the different transport paths exercised for mass transfer. These mechanisms help explain the process of sintering, densification and grain growth as a result of mass transport. There are two basic classes of transport mechanisms: surface transport and bulk transport. In surface transport, the mass originates from and deposits at the surface. It is mainly responsible for the neck growth at the interface without causing any change in particle spacing but plays no part in densification. Bulk transport mechanisms are the ones responsible for shrinkage. In these, mass moves from the interior of the particle to the neck, gradually eliminating the pores in process. These transport mechanisms are highly dependent on temperature. Out of the two, surface transport is dominant at low temperatures as it requires less energy for surface motion whereas bulk transports dictates sintering at high temperatures.

Each of these two basic mechanisms is further subdivided into three mechanisms making a total of six. The mechanisms are listed in table 2.1 [6]. All six of them are responsible for neck growth and bonding between particles but only the latter three lead to shrinkage. Figure 2.2 shows different types of transport mechanisms and the movement of mass from its source to final destination (sink) at the neck. [7]

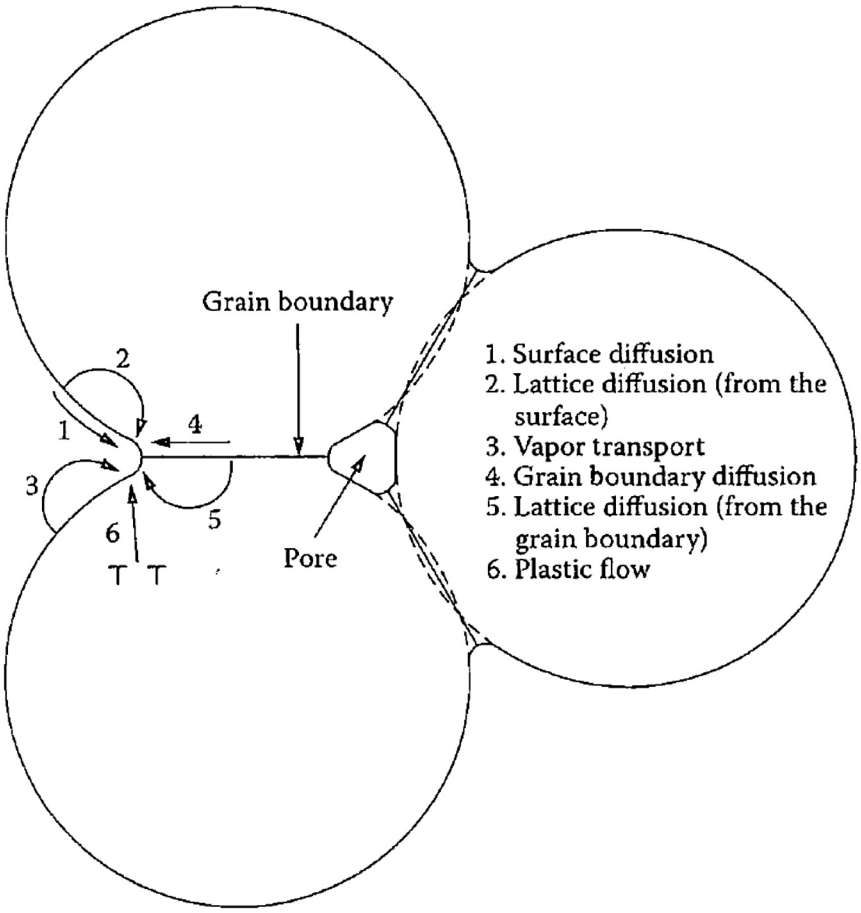

Figure 2.2: Distinct mechanisms of sintering

Mechanism	Transport Path	Source	Sink	Densifying
1	Surface Diffusion	Surface	Neck	No
2	Lattice Diffusion	Surface	Neck	No
3	Vapour Transport	Surface	Neck	No
4	Boundary Diffusion	Boundary	Neck	Yes
5	Lattice Diffusion	Boundary	Neck	Yes
6	Viscous Flow	Dislocation	Neck	Yes

Table 2.1: Mechanisms of sintering [6]

(1) Surface Diffusion: Surface diffusion occurs by movement from surface of the spherical particle to neck. It results in no shrinkage.

(2) Lattice Diffusion (surface): Diffusion of surface mass occurs through crystal structure instead of surface. Since the source and sink of mass is the surface, there is no densification.

(3) Vapor Transport: It results in transport of atoms from the surface to the neck by evaporation followed by condensation respectively. It only happens when the mean free path of an atom is greater than the distance between the regions.

(4) Grain Boundary Diffusion: As the activation energy required for it lies in between surface (lower) and lattice diffusion (upper limit), it is the most preferred mechanism in crystalline solids. Diffusion occurs through the grain boundaries to the neck (sink).

(5) Lattice Diffusion (boundary): Here, diffusion of atoms originates from grain boundaries through the crystal structure occurs. It is only possible if the grain boundary is under compressive stress and the neck is under tensile stress [8].

(6) Viscous Flow: This mechanism occurs in sintering of viscous or amorphous materials like glass. This mechanism does not occur in crystalline solids.

Hence, for crystalline solids, grain boundaries play an important role in sintering as shown by experiments of Alexander and Balluffi [9]. From table 2.1, when the neck growth begins due to the first three mechanisms, pores form interconnected channels for vacancy or mass transport as shown in figure 2.2. Eventually, these channels are shut giving isolated pores. These pores shrink or expand depending on grain boundary and surface energy. This grain boundary structure is described by dihedral angle. Dihedral angle is the angle made by the equilibrate between solid-solid interfacial energy and solid-vapor interfacial energy which is given by equation 2.3. [4]

$$\gamma_{ss} = 2\gamma_{sl} \cos\left(\frac{\varphi}{2}\right), \tag{2.3}$$

where, γ_{ss} is the solid-solid interfacial energy, γ_{sl} is the solid-vapor interfacial energy, and φ is the equilibrium angle. This dihedral angle determines the stability of pores and is calculated depending on the number of particles in contact with the pore [10]. Since the sum of all the dihedral angles for corresponding pore should give π, each dihedral angle is π/n. In case of a pore surrounded by 3 particles like in figure 2.2, it is $\pi/3$ and if it greater than $\pi/3$, the pore shrinks (convex surface) and vice-versa (concave surface) as soon as the dihedral angle is achieved.

2.1.3 Stages of Sintering

Sintering occurs in four sequential stages out of which stage 0 is just making of a green sample developing small particle contacts. Then, the following three stages are the main players in sintering. A common assumption made in all three stages is that there is no grain growth during sintering. Figure 2.3 shows the change in relative density with time for different stages of sintering [7, 11]

- **Initial Stage**: It is characterized by neck formation and neck growth and is also described by a two-particle model. Lattice, surface diffusion, and vapor transport are largely responsible for neck growth. Individual particles are still distinguishable in this stage as it only leads to neck formation. It results in only about $2-3\%$ of shrinkage.

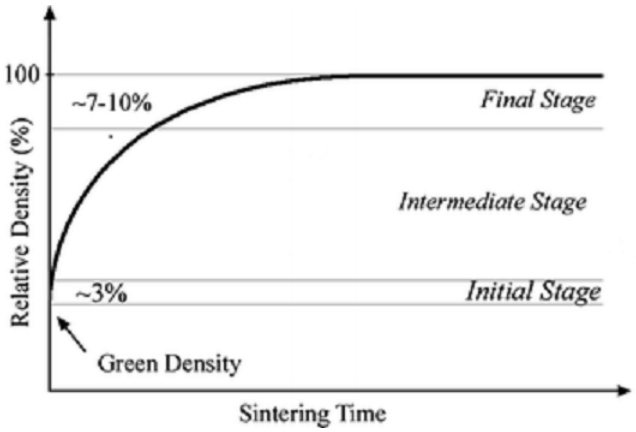

Figure 2.3: Different stages of sintering [7]

- **Intermediate Stage**: There is significant neck growth and densification in this stage. Inter-particle pore channels are formed for mass transport .These pore channels are assumed to be cylindrical, running along grain boundaries making it the most responsible mechanism for densification in this stage. Channel pore model describes this stage with an assumption of equal radial shrinkage. Majority of the mass transport happens in this stage giving a relative density of about 93% .

- **Final Stage**: The intermediate stage eventually leads to closure of the pore channels isolating the pores. An isolated pore model describes densification in this stage. Pores keep on shrinking until a balance in energies has reached. Further shrinkage only takes place if there is grain growth and if pores coalesce. Relative density of about $97 - 99\%$ is achieved at the end of this stage.

2.1.4 Methods of Sintering

Sintering is highly dependent on several factors which include material and extrinsic as mentioned in 2.1.1. When green bodies are made, they tend to have large defects which grow as densification proceeds. These non-uniformity in defects causes differential densification. Thus, small sized powders are preferred. In order to take advantage of various sintering parameters and avoid differential sintering, different methods are used to get densification while avoiding coarsening of the microstructre at the same time. Some of the widely used methods are discussed in brief.

- **Pressureless Sintering**: It is the traditional method of sintering a green body without any external applied pressure. Different heating schedules: constant-rate heating (CRH), rate-controlled sintering (RCS), and two-step sintering (TSS), can be performed to get different properties. CRH involves heating the compacted powder at a constant rate up to the sintering temperature. RCS varies the densification rate with time and essentially lowers it during the last stage. TSS uses two stages or two temperatures for sintering.

First, the sample is heated to the higher temperature and once the relative density is over 75%, it is switched to a lower temperature until full densification. This allows a much refined grain size than the previous two schedules. Although pressureless sintering produces uniformly sintered body, it requires high temperature and long time to sinter a body.

- **Pressure-Assisted Sintering**: External pressure is applied throughout the entire process increasing the overall driving force/potential and hence, reducing both the time and temperature needed for sintering. The external pressure helps in reducing the probability of having large packing defects or flaws by forcing the material, producing a more uniform distribution and reduced grain growth [12]. Hot pressing (HP) and hot isostatic pressing (HIP) are the two different ways in which pressure can be applied. HP involves the application of pressure unidirectionally with the powder inside a graphite die while HIP involves the application of a higher pressure in an encapsulated container in an inert atmosphere. Grain boundary and lattice diffusion along with plastic flow and creep are the possible sintering mechanisms highly relying on the applied pressure, temperature and particle size. Eventually, the sintering kinetics depend on pressureless sintering eliminating the role of external pressure. Also, the densification rate in this case is the sum of all the rates due to different mechanisms. The configuration for HP and HIP systems are shown in figure 2.4.

- **Microwave Assisted Sintering**: Microwaves or microwave energy is used to assist the process of sintering. Microwaves of frequency range 300 MHz-300 GHz are used for sintering. In this, heat is produced internally by coupling with the material [13, 14]. These microwaves result in motion of charges and rotation of dipoles at the molecular level where the resistance to respective movements results in heat. Here the thermal energy is transferred from the interior to the surface heating the specimen inside out unlike in conduction, radiation or convection and hence is hotter inside. When coupled with

conventional sintering, it results in rapid heating rates, energy consumption, and sintering temperatures. This leads to a more homogeneous temperature across the powder compact. Because of the rapid sintering rate, specimens show improved mechanical and physical properties with smaller grain size. Despite all the advantages, not all materials couple well with microwaves and in some cases, it can also lead to a phenomenon called thermal run-away. Also, it is difficult to use it for larger sample introducing non-homogeneous temperatures in the body.

- **Spark Plasma Sintering**: SPS has been one of the most successful methods for sintering compact powders. It is a process in which an electric field is used to assist sintering. It employs a very similar setup to pressure-assisted sintering. The setup consists of two graphite punches which apply pressure all throughout the process with a graphite die as seen in figure 2.4. Unlike conventional sintering, densification happens in a matter of minutes instead of hours due to very high heating rates (up to 1000 $^{\circ}C$ per minute) [15] at lower sintering temperatures. Because of very high heating rates, it can produce nanograin sized bodies that exhibit excellent mechanical properties. This high heating rate is a result of large amount of pulsed direct current (about 10kA) passing through the graphite die. Hence, this method is also known as pulsed electric current sintering, causes joule heating in the specimen. It is believed that high heating rates create an electric discharge (sparks) at the microscopic level generating a plasma but is yet to be confirmed as demonstrated by Hulbert [16]. Despite its exceptional properties, SPS is limited by the die geometry for compacts.

- **Flash Sintering**: This is the most recent sintering method discovered by Cologna, Rashkova and Raj [17] at the University of Colorado Boulder. In this compact powders sinter in as quickly as 5 seconds under an applied electric field which in turn acts as an onset for flash. This method is the main topic of discussion in this thesis and will be discussed in more detail in the upcoming section.

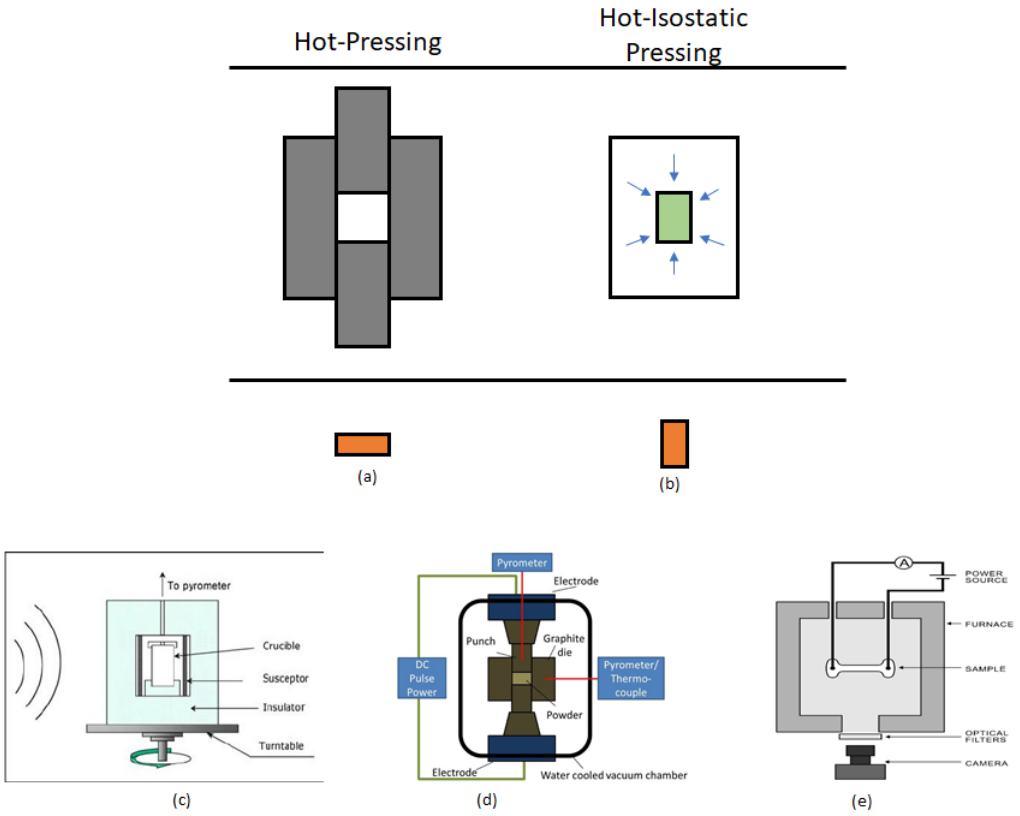

Figure 2.4: Types of sintering. a) Hot-Pressing, b) Hot-Isostatic Pressing, c) Microwave sintering, d) Spark Plasma sintering, e) Flash sintering

2.2 Flash Sintering

As mentioned before, flash sintering was discovered in 2010. This phenomenon involves rapid densification of a ceramic material in seconds under the application of an electric field at a certain onset temperature. During flash sintering, sample experiences glowing along with rapid densification i.e., it emits electroluminescence and its intensity is largely dependent on the current flowing through the sample. Three things that separate out flash sintering from other sintering phenomena are: (i) rapid densification, (ii) nonlinear rise in conductivity of the material, (iii) Electroluminescence of material. While most metal oxides flash sinter,not all materials exhibit this phenomenon, for example, alumina (without doping) does not show flash behavior despite of being a metal oxide [18]. While the mechanism responsible for flash sintering is still

under heavy debate, several possible explanations have been considered. The material of interest for this thesis was the one that flash sinters, 3YSZ in particular.

Just like conventional sintering has different stages as seen in figure 2.3, the entire flash sintering phenomenon can be divided into three stages, namely:

- **Stage I**: Stage I or the incubation time is the phase before the start of non-linearity. It is the time taken to reach the onset of flash. This stage sees a steady (linear) rise in current passing through the material at a specified electric field. The length of this incubation period is inversely proportional to the electric field applied across the electrodes and also the temperature of the sample. Hence, higher the electric field or temperature, shorter is the incubation period and vice-versa. This stage is responsible for increasing the temperature of the sample by joule heating till the flash onset point is reached. Also, stage I only results in little densification as seen in figure 2.5.

- **Stage II**: Stage II or the nonlinearity phase is when a sudden surge in conductivity of current occurs. This stage is a result of an intrinsic change in the specimen and is not influenced by any of the external factors like temperature, field etc., once this phase has reached. If this stage is not kept in check using a current limit, it can lead to lead to thermal and electrical runaway destroying the sample. This stage experiences the maximum amount of densification as visible by high relative density in figure 2.5

- **Stage III**: Stage III or the dwell state is the one in which sample reaches the set current limit and held steady in this condition. Full densification is accomplished in stage III but is also dependent on the current limit and dwell period. Higher the set current limit, higher is the relative density and the same goes for the dwell time until an equilibrium is reached.

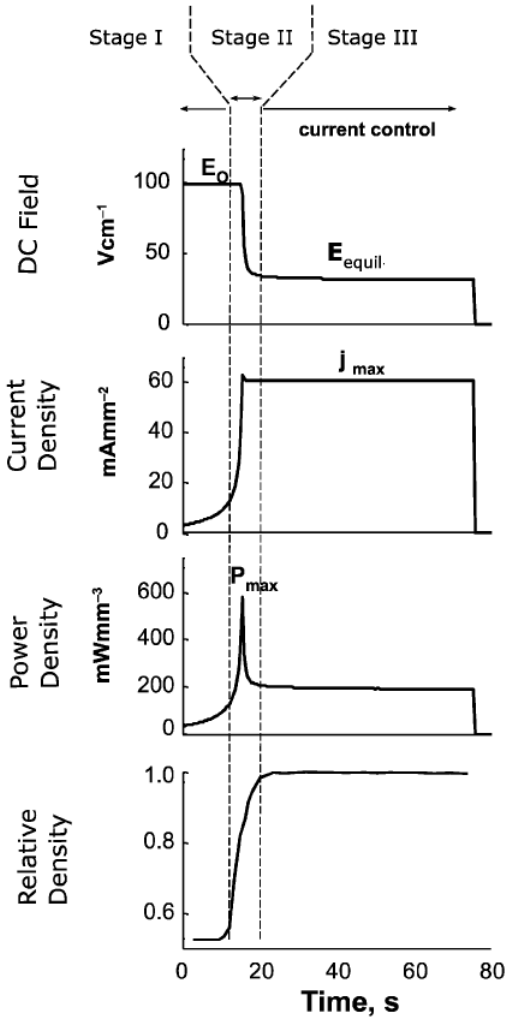

Figure 2.5: Different stages of flash sintering [19]

2.2.1 Setup and Process

A proper setup is needed to flash sinter a material which is shown in figure 2.4. It is a simple setup which requires a high temperature furnace, a power supply with the desired power rating, wires (preferred platinum due to its high melting point and low resistance), a high resolution camera with optical filters for dilatometry. A dogbone shaped sample is preferred as it is free of any external forces which allows free shrinkage. Two types of process can be used for flash sintering, which are voltage controlled and current controlled. These processes can be used for

three different types of experiments.

2.2.1.1 Constant Heating Rate Process

Constant Heating Rate (CHR) experiments are the first set of experiments to be done when trying to flash sinter new materials. The process involves heating up the sample at a constant heating rate, usually $10°Cmin^{-1}$, with an applied electric field. The furnace is set to the highest possible limit and the voltage and current are monitored through a MATLAB program. The experiment is continued until the sample flashes and the moment stage II begins (nonlinearity in current), temperature of the sample is recorded. This experiment is repeated for various electric fields (from low to high) and the temperatures are recorded for the same after which the plot of temperature vs electric field is generated. Yadav and Raj showed that after a certain temperature, there is no effect of electric field (generally very high electric fields) on the onset temperature for flash [20]. They found that this limiting temperature is the Debye temperature and is the lower bound for the onset of flash. This can be seen in figure 2.6. This onset temperature plot is then used to determine the required electric field for the onset of flash at a desired temperature and vice-versa.

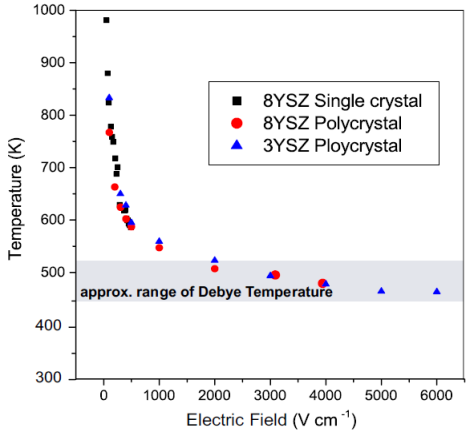

Figure 2.6: Temperature vs Electric Field

[20]

2.2.1.2 Isothermal Voltage Control Process

Where CHR is used to determine the onset temperature and required field, Voltage Control (VC) process is used to actually flash sinter materials. In this case, the furnace is ramped up to a desired temperature and is held constant at that temperature. Then, electric field is found using the onset temperature plot from CHR experiments and the value is set. Once the sample reaches the set temperature, the electric field is applied and a current limit is set. Once the field is applied, current starts to flow and the sample flashes reaching stage III and is dwelt in this state for a set time and then the field is switched off. Electric field and current limit are the controlling parameter for this process where the field is responsible for the onset of flash and current limit to avoid electrical runaway. The set current limit is the deciding factor in the densification of a sample and increases with the increasing current limit.

2.2.1.3 Isothermal Current Control Process

In Current Control (CC) process too, isothermal conditions are used to flash a sample. The major difference between CC and VC is that current is controlled from the very beginning in case of CC. This is done by setting a current rate for the process using a Matlab program in which, stage II or the nonlinearity phase is no longer present and current rises linearly until the current limit is achieved. The advantage of this process is that it provides better handle over the sintering process but at the same time, the sintering in a few seconds is no longer possible (depending on the current rate).

2.2.2 Effect of change in parameter

It was concluded that of all the parameters (temperature, electric field, and current density), current density affects the material properties like grain size, relative density, etc. Temperature and electric field only have an influence on the onset of flash and not material properties. Relative

density of the sample is highly dependent on the current density and keeps on increasing until a saturation is reached (density wise). Both, dwell time and current density in stage III, largely influences the grain size of a dense sample . It has been seen that the grain size is within $200nm$ range for a dwell time of less than 30 seconds but also keeps on increasing linearly for increasing current densities. This characteristic is observed in VC experiments.

The micro structure in case of VC experiments can differ. one reason for this could be due to the metal-ceramic interface resistance. Current control experiments seem to control this variation as the current rises slowly through the sample instead of a sudden nonlinear surge. The difference can be seen in the microstructure of CC flash sintered samples [21]. This is because of a more continuous sintering over a longer time span than a rapid densification rate. Also, it was concluded that CC gives more homogeneous relative density and also, a very small grain size. Other unusual effect of flash was a reversible phase change when a sample was kept in stage III for a long time. However, this phase change was only temporary [22].
Flash sintering has emerged as a really exciting field of study in terms of science and its applications, the very recent being reactive flash sintering where it is used for forming ceramic materials from different material oxides during flash in a very efficient way [22].

2.3 Natural Frequency of Vibration

Vibration is a phenomenon where an object undergoes oscillations about an equilibrium point. These oscillations can be periodic or non-periodic depending on the system. Vibrations usually are undesirable as they lead to a loss of energy in most cases. At the same time, they contain a lot of information about the system and can be helpful in understanding it. This work capitalizes on this information to look at the frequencies of vibrations from which stiffness is determined.

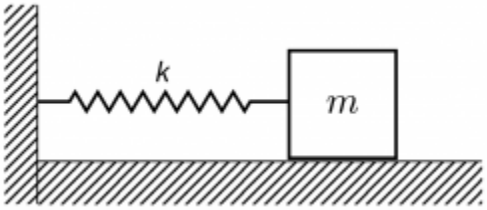

Figure 2.7: Spring-Mass System

2.3.1 Simple Harmonic Motion

The best example to describe a simple harmonic motion (SHM) is a spring-mass system. If an ideal system with no energy loss is assumed, if given an impulse, the mass will keep on oscillating forever. The spring mass system can be seen in figure 2.7 with the spring having a stiffness k and mass of the body m. When the object is given an initial displacement A, the force applied by the spring on the mass is a product of k and x. Once released, the mass keeps oscillating with a maximum displacement A. This spring force corresponds to the product of instantaneous acceleration and mass using Newton's second law of motion. Following are the equations of motion:

$$x(t) = A\cos(\omega_n t)\ , \tag{2.4}$$

$$ma = -kx \Rightarrow m\ddot{x} = kx, \quad \therefore m(A\omega_n^2\cos(\omega_n t)) = k(A\cos(\omega_n t)) \Rightarrow \omega_n = \sqrt{\frac{k}{m}} \tag{2.5}$$

The final relation shows that the oscillation frequency of the mass is independent of external factors and is an intrinsic property of the system directly proportional to the square root of the stiffness and inversely proportional to the mass. This ω_n is the natural undamped circular frequency of the mass/system. It is this intrinsic property of vibration which is used in this thesis to find the stiffness or rather the elastic modulus of the material.

2.3.2 Euler-Bernoulli beam theory

This section discusses the Euler-Bernoulli beam theory since the experiments in this thesis are performed using a cantilever beam. The concept remains the same as the one mentioned in section 2.3.1 and the final relation obtained here is considered as an extended version of equation 2.5. Bernoulli beam theory is used instead of Timoshenko beam theory due to very small displacements. A dynamic beam model is considered for this case as the beam undergoes oscillations. The dynamic beam equation from the Euler-Lagrange equation conserving the total energy of the system is given by:

$$S = \int_0^L \left[\frac{1}{2}\mu \left(\frac{\partial w}{\partial t} \right)^2 - \frac{1}{2} EI \left(\frac{\partial^2 w}{\partial x^2} \right)^2 + q(x)w(x,t) \right] dx \tag{2.6}$$

Here, the first term denotes the kinetic energy of the system where μ is the mass per unit length; the second term refers to internal potential energy where E is the elastic modulus, I the second moment of inertia, w the deflection in z direction; the third term represents the potential energy due to a continuous external load $q(x)$. For the system to have minimum energy, the Euler-Lagrange equation determines the following function:

$$\frac{\partial^2}{\partial x^2} \left(EI \frac{\partial^2 w}{\partial x^2} \right) = -\mu \frac{\partial^2 w}{\partial t^2} + q(x) \tag{2.7}$$

Since the experiments performed in this thesis involve an impulse, the external load $q(x)$ is 0. Hence, the general solution for the equation is given by:

$$w = A_1 \cosh(\beta x) + A_2 \sinh(\beta x) + A_3 \cosh(\beta x) + A_4 \sinh(\beta x) \ , \tag{2.8}$$

where $\beta = \left(\frac{\mu \omega^2}{EI} \right)^{1/4}$. Using the boundary conditions to solve, the final relation is achieved for different mode shapes. The first natural frequency is given by:

$$\omega_1 = \beta_1^2 \sqrt{\frac{EI}{\mu}} = \frac{3.5161}{L^2} \sqrt{\frac{EI}{\mu}} \ , \tag{2.9}$$

2.3.3 Damping of a system

All the above mentioned equations are valid in an ideal system where there is no loss of energy. However, energy is lost to the surroundings in the form of heat because of various factors.

Therefore, all oscillations eventually come to a stop unless the system experiences a load at all times. Damping is also responsible for changing oscillating frequency and this new frequency is nothing but damped natural frequency and is represented by ω_d. This is because damping reduces the oscillation rate by opposing the motion oscillating at a lower than expected. Depending on the value of the damping coefficient (ζ), a system can either be a/an: (i) Under-damped system ($\zeta < 1$), (ii) critically damped system ($\zeta = 1$), and (iii) over-damped system ($\zeta > 1$). Of the three, an under-damped system is observed in the studied experiments. A damped system is represented by adding a dash pot to the spring system shown in figure. 2.7. Hence, the new equation of motion is given by:

$$kx + \lambda\dot{x} + m\ddot{x} = 0 \Rightarrow \frac{m}{k}\frac{d^2x}{dt^2} + \frac{\lambda}{k}\frac{dx}{dt} + x = 0 \tag{2.10}$$

The final solution for this equation is given by:

$$x(t) = exp(-\zeta\omega_n t)\left\{x_0\cos(\omega_d t) + \frac{v_0 + \zeta\omega_n x_0}{\omega_d}\sin(\omega_d t)\right\}\ , \tag{2.11}$$

where $\omega_n = \sqrt{\frac{k}{m}}$, $\zeta = \frac{\lambda}{2\sqrt{k}m}$, and $\omega_d = \omega_n\sqrt{1} - \zeta^2$.

The above mentioned equations were used to find the corresponding values of undamped natural frequency.

2.4 Bond Energy, Elastic Modulus, and Activation Energy

Most material properties of different compounds, materials and even their phases depend on the bonding between the respective atoms and molecules. Elastic modulus, for that matter, is highly dependent on the bonding energy (even type of bond). Metals, ceramics, and polymers have varying properties. Brittle behavior exhibited by most ceramics is due to their high elastic moduli. Because of such high modulus, it is difficult for generation of point defects (especially vacancy, and self-interstitials) and hence, having a higher activation energy for the same. This section talks in detail about the relation between bonding energy, bonding length, modulus, and energy of formation of defects.

2.4.1 Bonding Energy

Metals, ceramics, polymers etc., can be differentiated from each other on the basis of type of bonding between them. There are two basic types of bonds: primary and secondary. Primary bonding takes place as a result of either electron sharing or transfer. They are further subdivided into: metallic, ionic, and covalent bonds.

- **Metallic Bonding**: As the name suggests, this is a bond that connects metal atoms. Here, valence electrons of the atoms sort of detach and form a big cloud of electrons which is evenly spread along the material space. It is because of this available electron cloud which makes metals highly conductive. Metallic bonds are really weak bonds.

- **Covalent Bonding**: In covalent bonding, sharing of electrons between the elements takes place in order to saturate the valence shell of each respective atom. Hybrid orbitals of each element overlap with each other to form a cloud containing electrons from both atoms. This is what makes them highly directional. It is much stronger than metallic but is also highly dependent on the localization of electron cloud in between them.

- **Ionic Bonding**: Ionic bonds are a result of electron transfer between atoms creating a positive (cation) or a negative charge (anion) ions. Coulomb force of attraction is responsible for holding them together and making a non-directional bond. Ionic compounds are usually hard, brittle, and insulators because of complete electron transfer and no shared cloud of electrons. Most ceramic materials are ionic materials and hence, have ionic bonds.

Since this study includes work on ceramics, bonding energy of ceramics (ionic bonding) is explained in detail. Along with Coulombic force of attraction, secondary forces (Van der Waals) also act upon these ions but as repelling forces. These secondary forces originate due to the overlapping of electron shells. However, the net force of attraction is represented by the sum of both

bonds as seen in equation 2.12. [23]

$$F_N(r) = F_C(r) + F_V(r) \ , \tag{2.12}$$

$$F_N(r) = \frac{z_1 z_2 e^2}{4\pi\epsilon_0 r} + \frac{B}{r^{n+1}} \tag{2.13}$$

where, F_C is the Coulombic force in which z_1, z_2 are the number of charges on each ion and e, and r represent the charge of a single electron and the distance between the ions respectively. F_V represents the secondary force which is dependent on the interaction of electron shells and varies from material to material.

The ionic compound reaches equilibrium when the opposing forces balance each other i.e., the net force is zero. The corresponding distance between the ions is the equilibrium bond length. Figure 2.8 shows the net force in an ionic material as function of distance. Here, note that on the left of r_0 the repulsive force exceeds the attractive force indicating that the ions are too close to each other and repelled by each other's electron cloud. Whereas on the right of r_0, Coulomb force dominates over repulsive force. Since, its much easier to interpret in terms of energy, the above equations are converted into an energy equation. Potential energy or the work done is given by equation 2.14.

$$U = \int F.dr \ , \Rightarrow U = -\frac{z_1 z_2 e^2}{4\pi\epsilon_0 r} + \frac{B'}{r^n} \tag{2.14}$$

Here, the equilibrium bond energy is the energy at distance r_0 where the net force is zero and can be seen in figure 2.8. This curve indicates the potential well where the bottom most point is the equilibrium bond energy. Hence, the more deeper the well goes, higher the stability of the compound as this is the minimum energy required to break the bond.

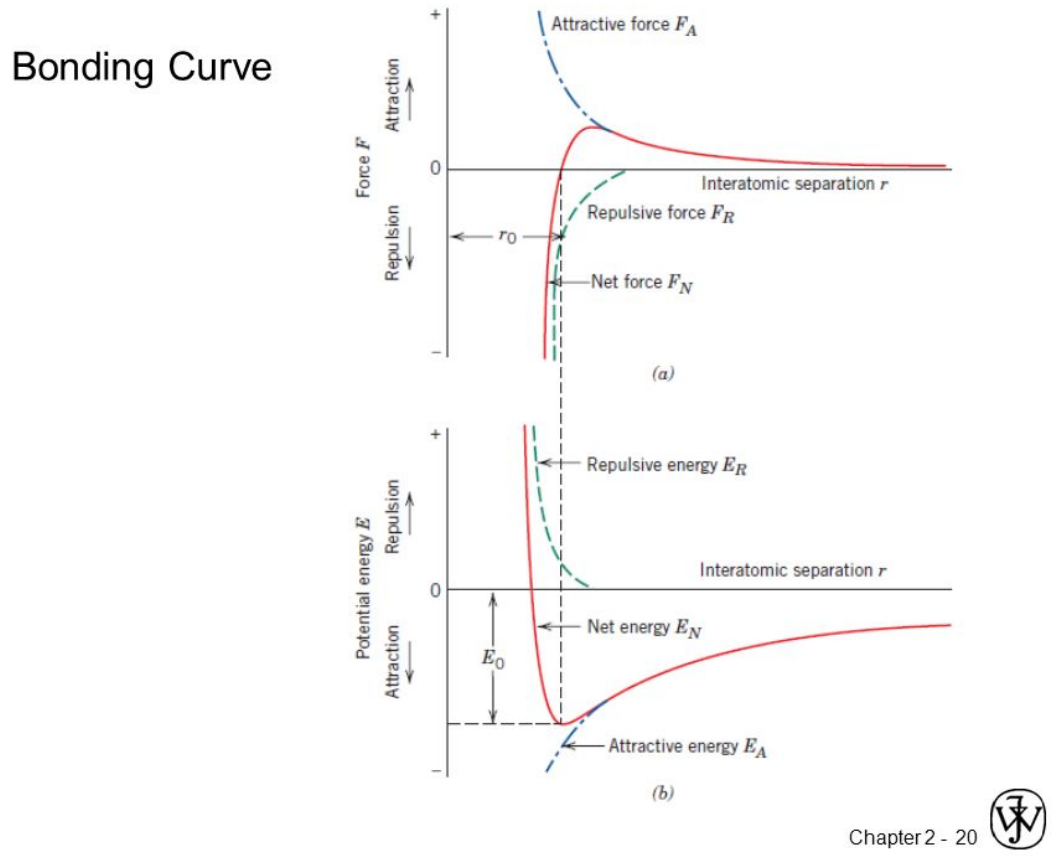

Figure 2.8: (a) The dependence of repulsive, attractive, and net forces on interatomic separation for two isolated atoms. (b) The dependence of repulsive, attractive, and net potential energies on interatomic separation for two isolated atoms. [23]

2.4.2 Elastic Modulus & Activation Energy

Bond or rather the bond energy is the basis of most mechanical properties including elastic modulus. In order to derive a relation between the two, an assumption that the material experiences small deformation is made allowing us to use the linear spring model. Now, if a small force is applied to stretch the ionic bond, the stress on the ion is given by:

$$\sigma = \frac{F}{A} = \frac{F}{r_0^2} = \frac{\frac{dU(r)}{dr}}{r_0^2} \tag{2.15}$$

This stress would lead to some strain ϵ. If r is the new ionic distance, strain is given by:

$$\epsilon = \frac{\Delta r}{r_0} = \frac{r - r_0}{r_0} \tag{2.16}$$

On dividing stress (σ) by strain (ϵ), a relation in terms of energy can be expressed.

$$\frac{\sigma}{\epsilon} = \frac{Fr_o}{r_0^2 \Delta r} = \frac{F}{r_0(r - r_0)} = \frac{\frac{dU(r)}{dr}}{r_0(r - r_0)} \tag{2.17}$$

Here, the applied force can be considered as a spring force and can be written in terms of stiffness, k and displacement Δr. However, it should be noted that this is only valid for very small deformations (less than 10%). Hence, the final equation is:

$$\frac{\sigma}{\epsilon} = \frac{k(r - r_0)}{r_0(r - r_0)} = \frac{k}{r_0} = \frac{\frac{dU(r)}{dr}}{r_0(\Delta r)} = \frac{1}{r_0}\frac{d^2U(r_0)}{dr^2} \tag{2.18}$$

$$E = \frac{k}{r_0} = \frac{1}{r_0}\frac{d^2U(r_0)}{dr^2} \tag{2.19}$$

Equation 2.19 gives a relation between bond energy, stiffness, and elastic modulus for small strains.This tells us that more stable a bond is, higher is the energy required to cause a small strain implying a higher elastic modulus (directly proportional from equation). Also, higher stiffness of the bond corresponds to a higher elastic modulus. Since ceramics, in general, have a very high elastic modulus, it points out that potential energy of the bond is really high.

Equation 2.2 is an arrhenius equation which gives the number of active atoms or the number of vacancies. Here, the vacancy generation is dependent on the activation energy, Q and temperature, T of the material. Activation energy, in this case, is defined as the energy required to generate a single vacancy which is nothing but the potential energy (U_0). U_0 is the energy required to move the ions an infinite distance away which in other words, is the energy to break free an ion since the Coulombic force tends to zero at infinity. High concentrations of vacancies can be achieved by heating the material to high temperature as at high temperatures, ions have higher thermal energy making it easier for them to make the jump over the activation energy. This leads to two types of intrinsic defects: Schottky and Frenkel defects of which Frenkel is highly probably as the activation energy required is quite low in comparison to Schottky defects.

$$n_f = (NN_i)^{1/2} exp\left(\frac{-\Delta H_F}{2RT}\right) \tag{2.20}$$

Equation 2.20 gives the number of Frenkel defects. Here, N is the number of lattice sites and N_i is the number of available interstitial sites. Frenkel defects occur in ionic solids where a vacancy is created at a lattice site and the same ion usually occupies an interstitial site in order to maintain an overall neutral charge. Here, ΔH_F is the activation energy to create a Frenkel i.e., the energy required to create a vacancy and an interstitial. Energy required to create an interstitial is much higher than for vacancy generation (about 3 times). Occupying an interstitial is very difficult as the neighboring atoms need to be pushed (compress the bonds) and ceramics, in particular, have very high compressive strength. Hence, an ion should be at a higher energy state to occupy an interstitial site. Therefore, the concentration of Frenkel pair is very less probable at low temperature and a few at high temperatures.

Hence, high elastic modulus paramounts to high activation energy and lower Frenkel concentrations.

Chapter 3

Objective

3.1 Scope

The goal of this work is to make in-situ measurements of mechanical properties, elastic modulus in particular, of dense 3Y-TZP under the state of flash using a non-destructive testing (NDT) method. Additionally, the effect of different flash lengths and varying current densities on elastic modulus and damping coefficient is examined. Another important aspect considered is the transience of these properties due to the influence of flash i.e., is the effect permanent or disappears after the flash event.

3.2 Significance

The mechanism behind the astonishing discovery of sintering most ceramic materials in a matter of seconds while maintaining mechanical properties is still under debate. This work offers good insight about the effect of flash on 3Y-TZP. The results observed from these experiments take a step towards understanding the underlying mechanism of flash sintering. They also confirm the suggestion of softening of elastic modulus during the state of flash due to unusually large displacements of atoms. It could also support the theory put forward about the creation of Frankel defects because of non-linear lattice vibrations during the flash phenomenon and how the creation of these Frankel pairs can soften the lattice.

Chapter 4

Experimental Method

4.1 Sample Material

All the experiments done in this study were carried out using rods made from 3mol% Yttria Partially Stabilized Zirconia (3Y-TZP). These fully dense rods were bought from CoorsTek. They constitute Zirconia, Yttria, Alumina, Titania and other impurities. The weight percentage composition of 3Y-TZP is as follows: ZrO_2 (94.2 wt%), Y_2O_3 (5.4 wt%), Al_2O_3 (0.25 wt%), TiO_2 (0.1 wt%) and other impurities (0.05 wt%). Rods of diameter 1.83 mm and length 6 inches were used for making the specimens. Alumina tubes from Coorstek (USA) with an internal diameter of 7.95 mm and external diameter 11.13 mm having a density 3.92 gm/cc served the purpose of rod holders.

Two different types of cement were used to cement the rod and an alumina tube. A 20 minute mud (powder) was followed by a high temperature cement, Omega Bond OB-600 (powder) by Omega in particular.

4.2 Sample Preparation

The entire sample preparation took about 48 hours in total. Before cementing the rod, density was calculated by measuring the mass, diameter and length of the sample. One side of the rods was then ground and polished to get a flat reflecting surface and two tiny notches were made at an equal distance from both ends to hold the platinum wires in place. As soon as the

notches were made, thin platinum wires (32 gage) were tightly wrapped around the sample and a platinum paste was applied at the wire rod interface to get better contact. It was then heated at a rate of $9°C$ per minute to $1200°C$ for about 2 hours to fuse them together.

Slurry of the 20 minute mud was filled inside the alumina tube and was kept in air for about 4-5 hours and then overnight in the oven at $80°C$ to harden the cement. A small hole was made in this cement to fix the rod. Then, a slurry prepared by mixing OB-600 and D.I. water in specified proportions was added around the rod. A 3-D printed support structure was used to keep the rod and tube in a vertical position. The slurry was then allowed to dry and settle down for about 18-24 hours at room temperature after which it was kept in the oven at $82.2°C(180°F)$ and $104.4°C(220°F)$ for about 4 hours each. Once the sample was ready, a small piece of reflective tape was stuck on the flat surface for accurate measurements.

4.3 Experimental Equipment

4.3.1 Frequency Measurement Experiment

This experiment examined the vibration signals of the cantilever beam using the setup shown in figure 4.1. An in-house made Platinum furnace of dimensions: external diameter- 51.5 mm, internal diameter- 9.53 mm and furnace height of 56 mm was used lab for high temperature (upto $1600°C$) experiments using alumina tubes. A Hewlett Packard DC power supply (6261B, 0-20V & 1-50A) was used to heat the furnace with a K-type thermocouple (Chromel/Alumel) to regulate the furnace temperature. An aluminum plate was machined to clamp the sample firmly.

Displacement-Time signals (vibrations) were collected by a Polytech Portable Digital Vibrometer (PDV-100). It uses a helium neon laser of wavelength 633 nm with a frequency measurement range from 0.5 to 20,000 Hz. It was kept at a distance of about 20 inches from the sample as proposed by Polytech in order to get optimal measurements. An impact hammer (PCB 086C02)

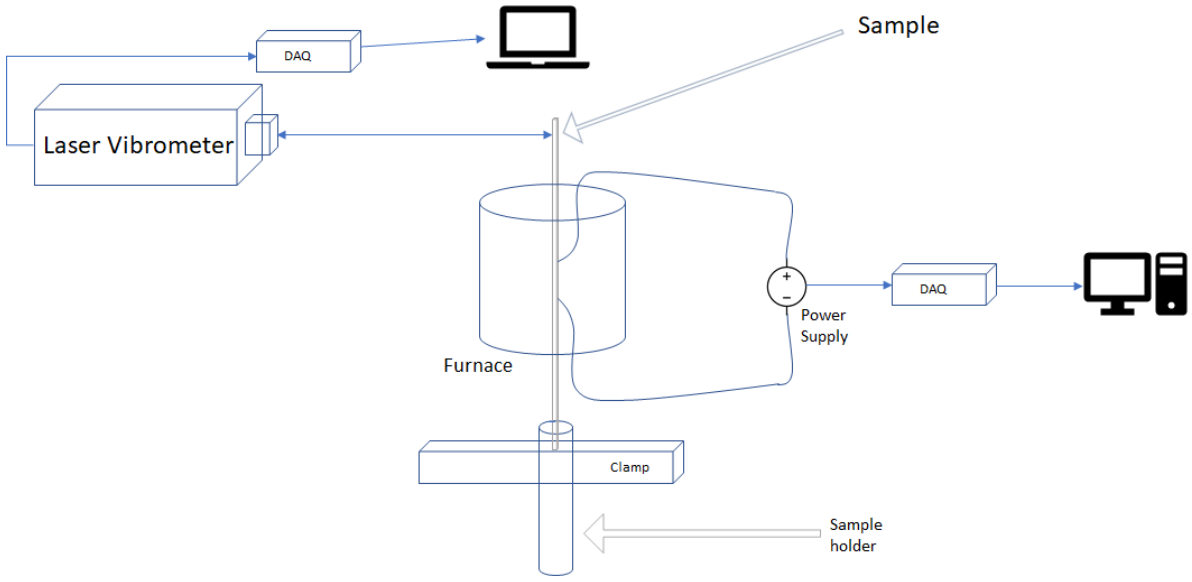

Figure 4.1: Experimental Setup

from PCB Piezotronics was used to give an impulse to the sample. A Polytech Data Acquisition System (VIB-E-220) was used to acquire data from both the Vibrometer and hammer. Vibsoft 5.3 and Vibsoft 5.3 Desktop (software) along with keys (VIBSOFT-20 and VIBSOFT-desktop) were needed to access the data on a computer.

Two platinum wires of gauge 32 were wrapped around the sample inside the furnace for flash. Electric power was supplied by a 600W DC power supply (Sorenson DLM 300-2). Current was measured by connecting a Digital Multi-Meter (DMM-Keithely 199) connected in series with the power supply. This analog output from the DMM was saved using a GPIB interface and a National Instruments USB-6008. Voltage and current data of flash were recorded into a single MATLAB and text file using MATLAB©.

4.3.2 Optical Pyrometer Measurements

Separate experiments were performed to measure the temperature of the specimen during flash. An infrared pyrometer, Micro-Epsilon optris©CT laser model- 1MH and focus CF4, was used. It consists of an infrared sensor for temperature estimation and a laser pointer to get a spot size. It has a temperature range of $650°C$ - $1800°C$ with a spectral range of $1\mu m$ with an optical resolution of 330:1 with variable emissivity from 0.100-1.100. For these experiments, emissivity was set at 0.900 due to material properties (3Y-TZP has an emissivity of 0.9). It has a spot size of 1.4 mm with a focal distance of 450 mm. Temperatures were displayed using an electronic box and recorded using a National Instruments X series USB-6363 via MATLAB on a computer.

4.4 Data Analysis

4.4.1 Room Temperature Elastic Modulus of 3YSZ

Room temperature elastic modulus played an important role in this study as it was the only known value which was later used for Finite Element Analysis. Modulus of the specimen

prepared in section 4.2 was calculated by the following equation 4.1:

$$\omega_n = \alpha_n^2 \sqrt{\frac{EI}{\rho A L^4}} \ , \tag{4.1}$$

where ω_n is natural circular frequency, α_n = 1.875, 4.694, 7.853. . . for n^{th} mode of vibration, E is the elastic modulus of the material, I is area of moment of inertia of the beam, ρ is the density, A the cross-sectional area, and L the length of a beam . In this equation, natural frequency is measured by performing the Fast Fourier Transform on the signal and calculating the damping coefficient of the same, which will be discussed in more detail in the upcoming subsections.

4.4.2 Fast Fourier Transform

Data acquired from the Vibrometer consists of displacement-time signals which, as shown in Figure 4.2a, demonstrates the behavior of the tip of sample over time. Performing a Fast Fourier Transform (FFT) on this signal gives a frequency distribution that constitute the signal. A Maltab©program was written to get the frequency distribution. Different damped natural frequencies are then extracted from this distribution for a single frequency as visible in figure 4.2b.

The natural frequency of vibration is calculated by using this damped frequency and damping ratio which will be discussed in the next section.

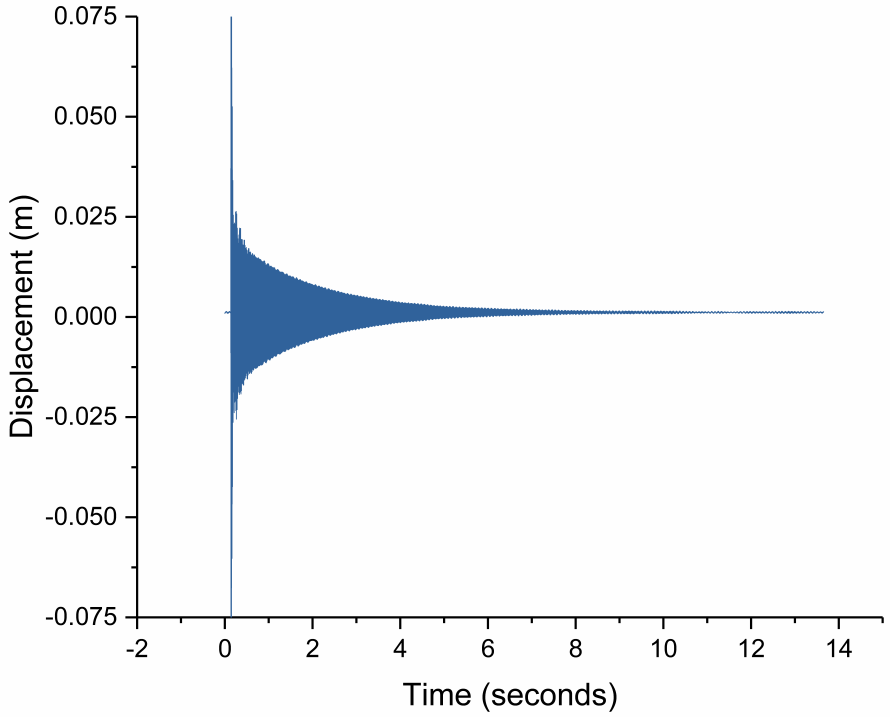

(a) Time domain signal

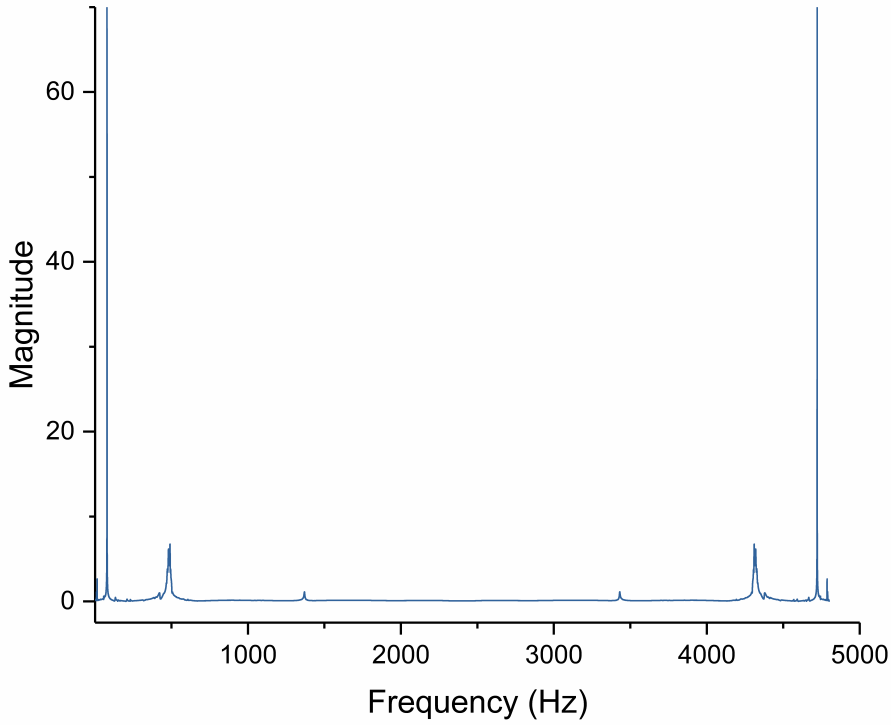

(b) Fourier Transform of time signal

Figure 4.2: Frequency Analysis of vibration

4.4.3 Damping Coefficient

The damping coefficient of a particular frequency was calculated by measuring the logarithmic decrement from the amplitudes of vibration. This logarithmic decrement was measured using two methods:

- **Amplitude ratio**: One way of calculating logarithmic decrement is by taking the natural log of the ratio of the amplitude of two neighboring peaks.Equation 4.2 is used to make these calculations. However, a more accurate way to estimate is by using the equation 4.3.

$$\delta = \ln\left(\frac{x(t_n)}{x(t_{n+1})}\right) , \tag{4.2}$$

$$\delta = \frac{1}{n}\ln\left(\frac{x(t_0)}{x(t_n)}\right) , \tag{4.3}$$

  where δ is logarithmic decrement, n is the number of cycles, $x(t_0)$ is the amplitude of first peak, $x(t_n)$ is the amplitude at n^{th} peak, and $x(t_{n+1})$ the amplitude of $n+1^{th}$ peak.

- **Full Width Half Maximum**: Logarithmic decrement in this case was estimated from the FFT plot of the time signal by measuring the Full Width Half Maximum (FWHM). A Gaussian fit was used to fit a peak. An exponential equation of n terms depending on fit was found. This equation was then used to find the width at half the maximum of the peak. Logarithmic decrement is then measured using equation 4.4. [24]

$$\delta = 1.814\frac{\Delta f_h}{f_n} , \tag{4.4}$$

  where Δf_h is the full half width of the frequency, and f_n is the nth mode of vibration.

The estimated logarithmic decrement is then used to calculate the corresponding damping coefficient. The equation for damping coefficient is given by equation 4.5

$$\zeta = \frac{\delta}{\sqrt{4\pi^2 + \delta^2}} \,, \tag{4.5}$$

where ζ (zeta) is the damping coefficient.

The first fundamental natural frequency of the sample is calculated by using the damped natural frequency and damping coefficient which is represented by the following equation 4.6

$$\omega_d = \omega_n \sqrt{1 - \zeta^2} \,, \tag{4.6}$$

where ζ is the damping coefficient, ω_d is the damped natural frequency, and ω_n is the undamped natural frequency.

4.4.4 Finite Element Analysis

Finite Element Modeling was done using SolidWorks©simulation. Figure 4.3 shows the sample used for FEM analysis. It is fixed on one end in all directions to represent the cement and material properties were set for different parts of the sample. Once ran, the simulation generated frequencies for different modes of vibration.

On left, is the original sample with fixed end and the one on right is the simulation snapshot of the sample under free vibration. In this, the elastic modulus of the boxed region was changed to obtain the behavior of natural frequency with elastic modulus.

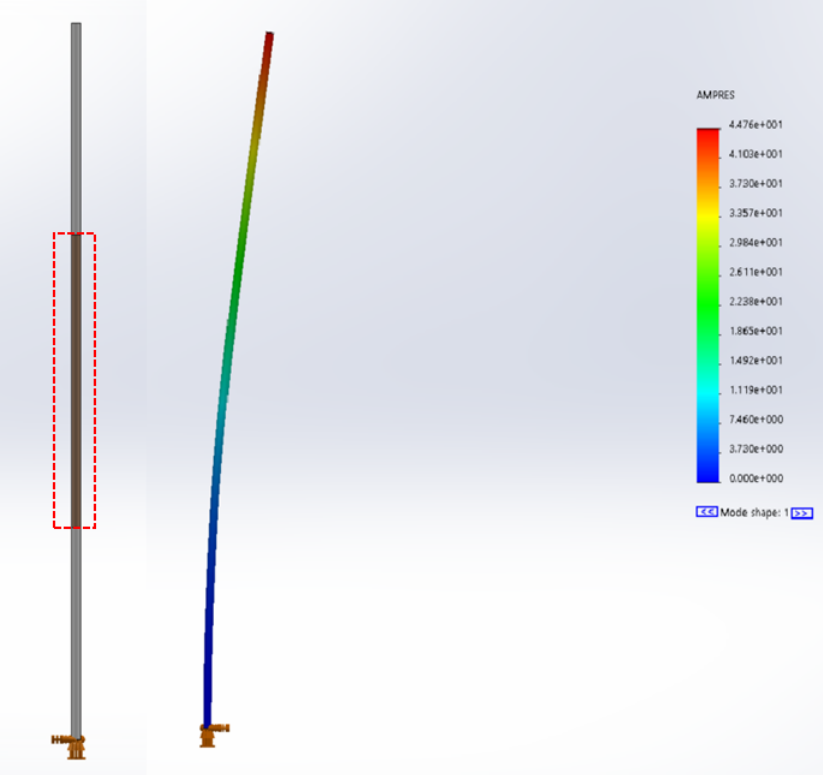

Figure 4.3: SolidWorks Simulation of the sample fixed at one end for first mode of vibration

4.4.5 Elastic Modulus at different temperatures

Elastic Modulus of 3Y-TZP as a function of temperature and also during flash was estimated by combining the results from sections 4.4.2, 4.4.3 and 5.1.2.2. Natural frequency was calculated using FFT of the time signal and equation 4.6. For this frequency, a corresponding value of elastic modulus was obtained from FEA. This process can be seen in figure 4.4.

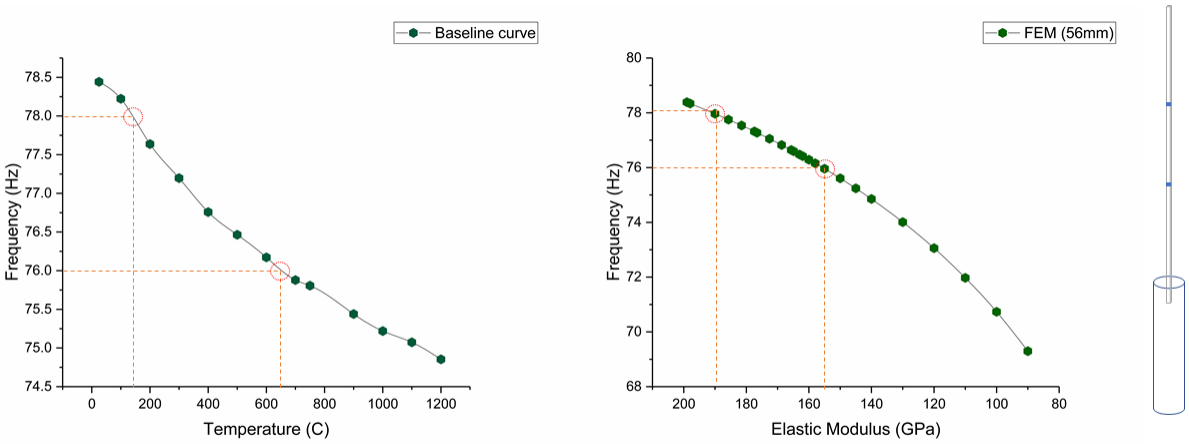

Figure 4.4: Extrapolating Elastic Modulus from experiment and fem

Chapter 5

Experiment

5.1 Temperature-Baseline (Furnace ON) experiment

Very few reliable sources for the elastic modulus behavior of 3Y-TZP as a function of temperature are available out of which papers by Shimada [25] and Adams [26] are referred. Hence, a reliable relation of elastic modulus with temperature of 3Y-TZP was required for this study and also compare the same with literature. This curve was also used as a baseline plot in an effort to measure the influence of flash-sintering behavior in 3YSZ and separate it from the effect of temperature.

5.1.1 Process

The specimen (cantilever rod) was prepared by the process mentioned in chapter 4. Markers for the top and bottom ends of furnace were made on the sample at equal distances from both ends of sample. A thermocouple or a temperature reader was inserted into the center of furnace to record its temperature. Markings on the sample were then matched with the furnace. It was oriented in such a way that the flattened portion of the sample was aligned perpendicularly with respect to the laser from the vibrometer. Once oriented correctly, the sample was clamped rigidly onto the aluminum plate in all four directions. Laser was then focused at a point on the free end of the sample.

An impulse hammer was used to impart motion to the sample while simultaneously measuring the magnitude of the impact. Data (vibration time signal) was acquired initially at room temperature ($25°C$) with and without the platinum wires in order to calibrate the signal for acquisition. Once calibrated, temperature of the furnace was raised in the multiples of $100°C$ at a heating rate of about $6°Cmin^{-1}$ with a dwell period of 15 minutes to evenly distribute temperature along the sample. It was also held at $750°C$ because this was chosen as the isothermal flash condition. Data was then collected at the end of each cycle upto $1200°C$. Each temperature data set comprised of six readings to obtain consistent data.

Acquired data was saved as a '.pvd' file (default extension of the data acquisition software) and then converted to a text file for further data analysis (time signals). As mentioned in section 4.4, data was analyzed to get the natural frequencies and eventually the elastic modulus versus temperature. These results will be seen in the next subsection.

5.1.2 Results

5.1.2.1 Undamped Frequency of Vibration

As mentioned in section 4.4, the time domain signal acquired from the vibrometer is converted into the frequency distribution pattern by Fourier transform and damping equations using Matlab©. Figure 5.1 shows the change in first fundamental frequency of the cantilever beam with temperature. It can be seen that there is a quick drop in frequency up to $300°C$ of about 0.5 Hz every $100°C$ and then gradually reducing to about 03 Hz at $1200°C$. From equation 4.1, Sample frequency is dependent on both the material (Elastic Modulus) and geometrical properties. Difficulty in maintaining the same geometrical properties largely caused the variation in frequency measurements. Other varying factor was the material itself, for example, a little change in density indirectly affected the frequency of vibration. Also, it was found that the change in frequency was very similar regardless of different samples. Hence, Δf was used to compare the different

samples as shown in figure 5.2.

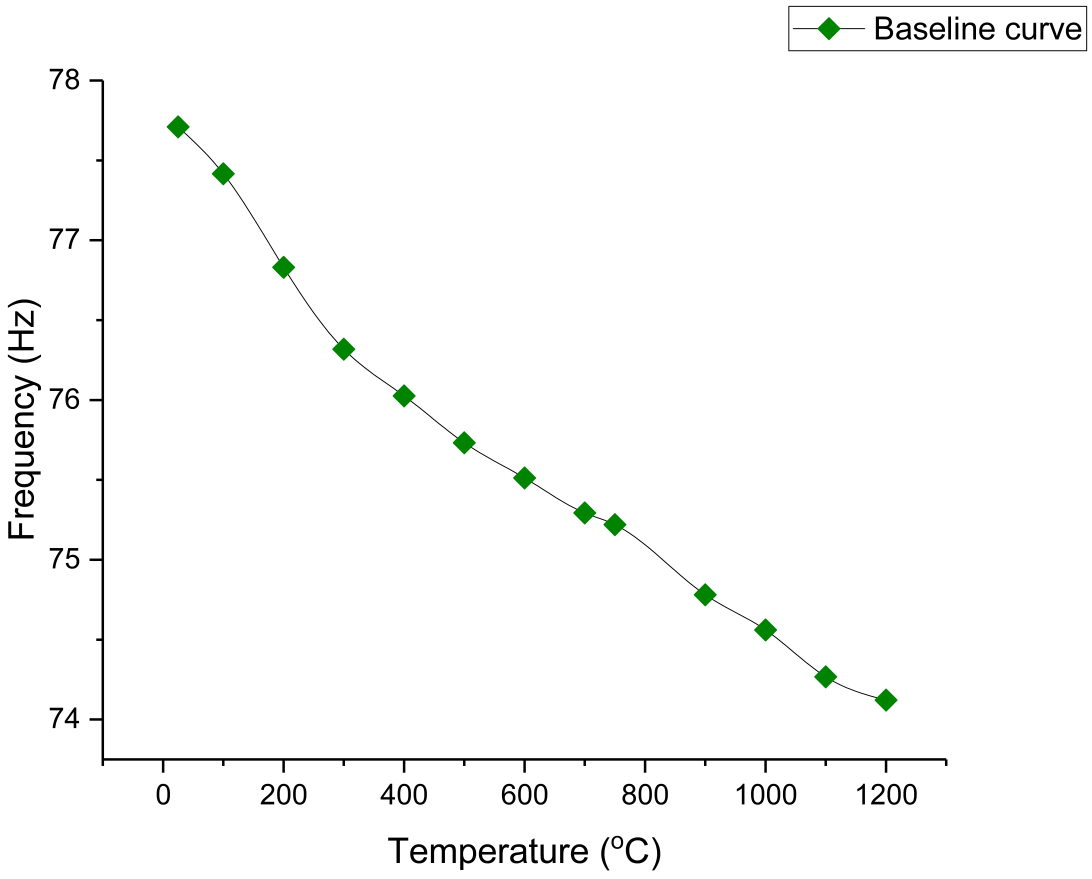

Figure 5.1: Frequency vs Temperature Response

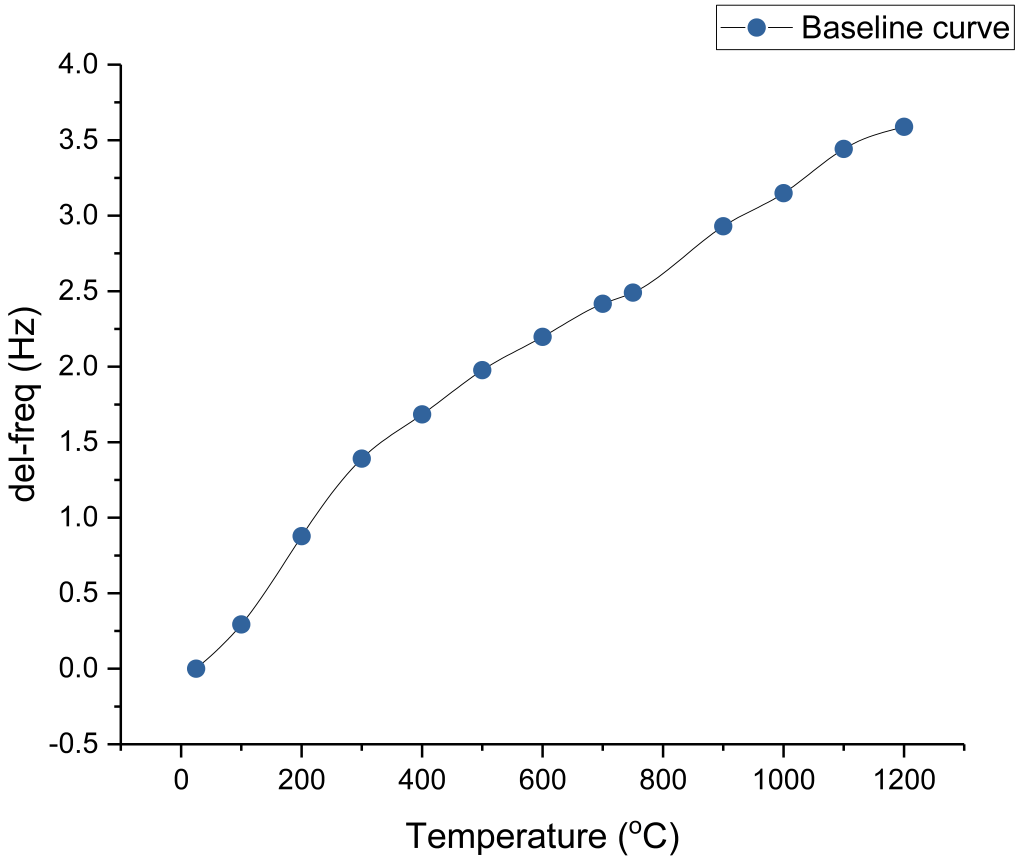

Figure 5.2: Δfrequency vs Temperature Response

Damping coefficient or zeta was estimated using the equations mentioned in section 4.4.3. Although, both methods gave similar values of logarithmic decrement, FWHM method was preferred as the values obtained from it could be singled out for different frequencies. Hence, giving more reliable values. The fft does not directly give the FWHM values. A Matlab©script was written to generate the best possible Gaussian fit. One of the fits can be seen in figure 5.3. Behavior of damping coefficient with temperature can be seen in figure 5.4. ζ was found to increase till $200°C$ to 0.0024 and then drops down to 0.0022 and is fairly stable up to $1100°C$ and then increases to 0.0031 at $1200°C$.The observed behavior was quite similar to the drop in frequency where it eventually stabilized corresponding a relation between the two.

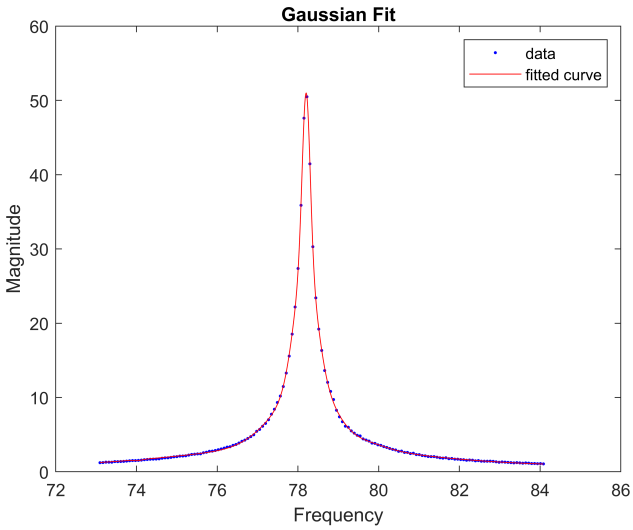

Figure 5.3: Gaussian Fit of first peak

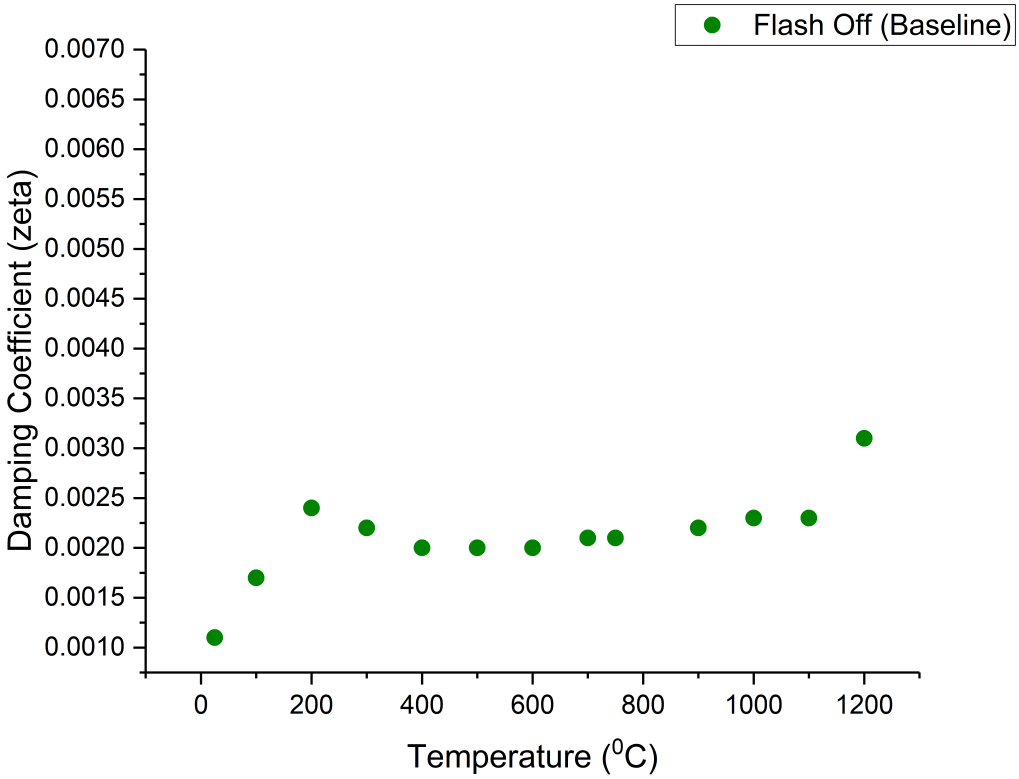

Figure 5.4: Damping Coefficient vs Temperature (Baseline data)

Undamped natural frequencies were then calculated using equation 4.6. Table 5.1 displays the change in natural frequency due to damping.

Temperature $(^{\circ}C)$	**Damped Frequency** (ω_d)	**Damping Coefficient** (ζ)	**Undamped natural frequency** (ω_n)
25	77.71	0.0012	77.71
100	77.417	0.002	77.4171
200	76.8311	0.0025	76.8313
300	76.3184	0.0023	76.3186
400	76.0254	0.0021	76.0256
500	75.7324	0.002	75.7326
600	75.5127	0.002	75.5129
700	75.293	0.0021	75.2931
750	75.2197	0.0021	75.2199
900	74.7803	0.0022	74.7805
1000	74.5605	0.0023	74.5607
1100	74.2676	0.0026	74.2678
1200	74.1211	0.0032	74.1215

Table 5.1: Frequency and Damping coefficient

5.1.2.2 Finite Element Method

For the baseline (furnace on and flash off) experiment, Finite Element Analysis was done for different elastic moduli of furnace. Room temperature elastic Modulus was calculated using the equation 4.1. This modulus was set for the outer regions on either side of the furnace for simulations. SolidWorks Simulation was used to get undamped natural frequencies for its respective elastic modulus and a plot for the same was obtained. At the beginning, the frequency drops slowly for reducing modulus but eventually frequency drops is considerable for a small change in modulus. Also, the relation between them seems quadratic which is noticeable from figure 5.5 and also from equation 4.1. Notice that the simulations were done under the assumptions that there was no damping in the specimen.

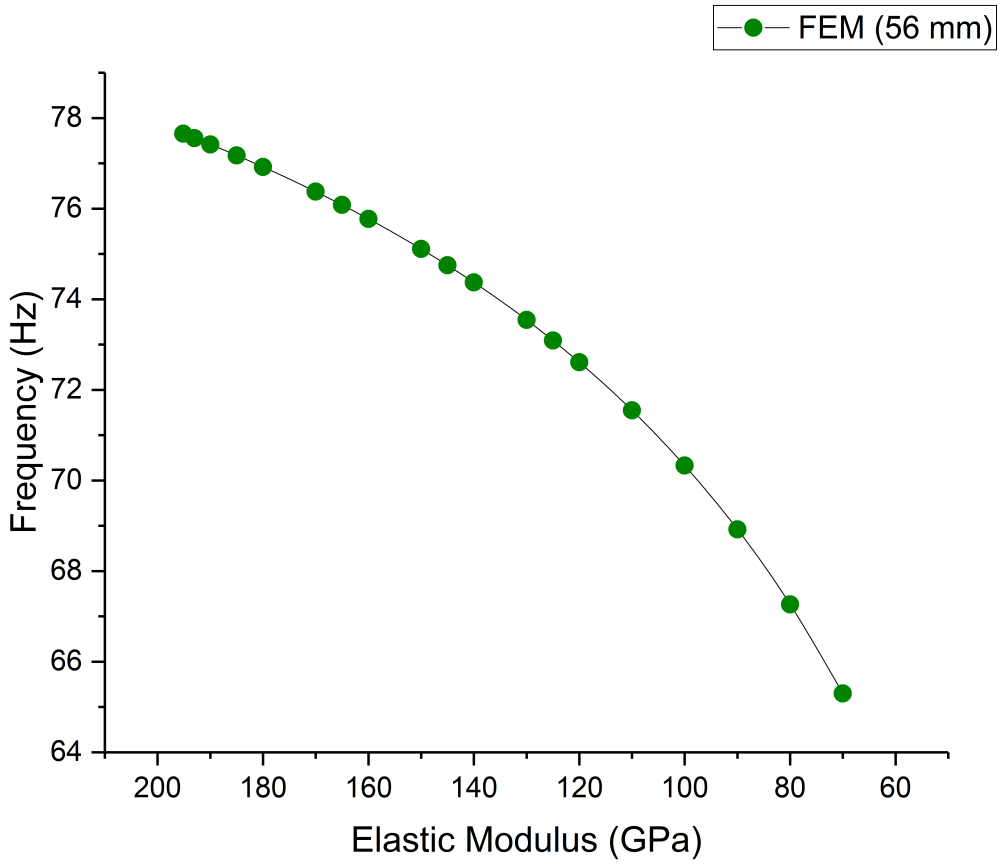

Figure 5.5: Finite Element Plot of Frequency vs Elastic Modulus

5.1.2.3 Elastic Modulus

A plot of elastic modulus with temperature was derived by the process mentioned in section 4.4.5. Since the simulations were done under no damping conditions, frequencies estimated from equation 4.6 were used for extrapolation. The plot of elastic modulus vs temperature can be seen in figure 5.6. On comparing the experimental plot with literature [26], it is noticed that the plot follows the same inverted 's' shape with a difference of about 15 GPa at $1200°C$. It was observed that the elastic modulus of 3Y-TZP changes drastically at low temperature, for example, room temperature modulus is about 200 GPa which drops down to 170 GPa at $400°C$. After $400°C$, a total drop of about 30 GPa is observed till $1200°C$ forming an inverted 's' shape. The reason for

observed deviation of experimental plot from literature will be discussed later.

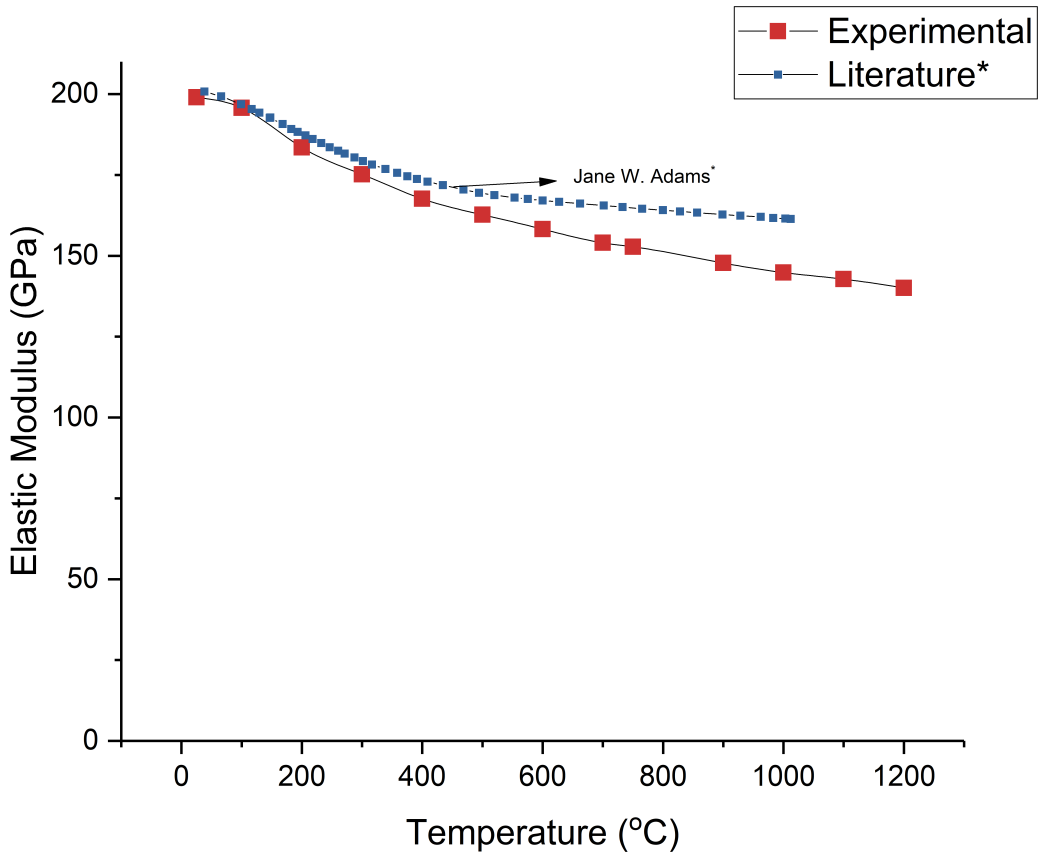

Figure 5.6: Elastic Modulus vs Temperature

5.2 In-situ flash measurements

As mentioned in chapter 2, flash sintering results in rapid sintering of ceramics (3Y-TZP) in seconds rather than minutes or hours. This section studies the in-situ elastic modulus of 3Y-TZP while maintaining the state of flash. In addition to understanding the effect of flash at different current densities, influence of different flash lengths (the region where the sample flashes) was also measured. The temperature of the flash length was measured by two methods: by using an optical pyrometer; By calculating the Black Body Radiation (BBR) temperature based on the

power density consumption. These temperatures were the links that connected flash and no flash estimations and were used for comparing the two as shown in section 5.1. This section mainly looks at the results of flash ON and furnace OFF measurements, i.e., the sample was still in flash condition while the furnace was cooling down.

5.2.1 Process

As soon as the measurements were made at $1200°C$, the furnace is slowly cooled down to $750°C$ at about $7°C\ min^{-1}$ and held for about 30 minutes for even temperature distribution. Vibrometer measurements were taken at this temperature to serve as a reference for the measurements made during flash. Since the connections to the power supply for flash were made at the beginning, the power supply for applying electric field and the Keithley for measuring the current were switched on. The value of electric field was set to $100V\ cm^{-1}$ in the Matlab program GUI and the current limit was set to different values as the experiment progressed. This value for electric field and temperature were chosen based on the onset values for flash found from the figure 2.6 [20]. The current densities at which the measurements were taken were $60mA\ mm^{-2}$, $80mA\ mm^{-2}$, $100mA\ mm^{-2}$ and $120mA\ mm^{-2}$. The flash was initiated by using lower current densities at the beginning to avoid cracks due to thermal shock experienced by the sample.

As soon as the first current limit was reached (required current density for measurements), it was held steady for about 10 to 15 minutes to stabilize the power density required. Then, an impulse hammer was used to record vibration measurements like in section 5.1.1. These steps were repeated for each current density. Once the measurements were recorded, the furnace was turned off while still maintaining the state of flash at a current density of $120mA\ mm^{-2}$. The basis for turning off the furnace was to eliminate the thermal effect of the furnace which made it harder to validate the results because of complex Finite Element Analysis. The furnace was then cooled down for about 150-180 minutes until the power density or rather the voltage needed to

maintain the same current was steady. Once this state was achieved, the measurements were recorded for the above mentioned current densities in the same way as when the furnace was turned on.

For temperature measurements using an infrared pyrometer, the exact steps as mentioned above were repeated but in a different setup. A horizontal split furnace was used to measure the temperature instead of the platinum furnace (in which vibration measurements were recorded) as the latter did not have a slit for pyrometer measurements.

The entire process mentioned above was performed for sample with different flash lengths of $10\ mm$, $20\ mm$ & $30\ mm$.

5.2.2 Results

5.2.2.1 Undamped frequency of vibration

Undamped natural frequency (1^{st} mode) for the sample under flash was obtained by performing the Fourier transform of respective time domain signals, obtaining the damping coefficient and using the equation 4.6. These steps are the same as performed in section 5.1.2. Table 5.2 displays the damping coefficient and the estimated natural frequency for different flash lengths: $10mm$, $20mm$, and $30mm$. Damping coefficient is plotted against the temperatures measured by the infrared pyrometer for corresponding current densities. Also, the thermal effect of furnace can be seen by the difference in damping coefficient, pyrometer temperatures and natural frequency with and without the furnace for each flash lengths. Even when the corresponding frequencies were monitored, an increase in the range of $1.4\ Hz$ - $1.7\ Hz$ was observed irrespective of current densities and flash lengths indicating successful elimination of the furnace.

Current Density	**Natural Frequency** (ω_n)		**Damping Coefficient** (ζ)	
$(mAmm^{-2})$	**Furnace On**	**Furnace Off**	**Furnace On**	**Furnace Off**
10 mm flash length				
60	74.8538	76.3918	0.0028	0.0023
80	74.7075	76.3186	0.0035	0.0028
100	74.4879	76.099	0.0042	0.0033
120	74.1954	75.8795	0.005	0.004
20 mm flash length				
60	75.0732	76.0986	0.0028	0.0026
80	74.4873	75.8057	0.0054	0.004
100	74.0479	75.3662	0.0072	0.0055
120	73.4619	74.8535	0.0094	0.0071
30 mm flash length				
60	74.9278	76.2454	0.0054	0.003
80	74.1966	75.7535	0.0078	0.0054
100	73.3199	75.0021	0.011	0.0075
120	72.6652	74.3445	0.0157	0.0104

Table 5.2: Furnace Effect during flash

5.2.2.2 Finite Element Method

This section involves the same process as section 5.1.2.2 where instead of the furnace length ($56\ mm$), different flash lengths ($10\ mm$, $20\ mm$, & $30\ mm$) for different samples were used, i.e., frequency response of the sample was observed when the elastic modulus of these lengths was changed. This is shown in figure 5.7.

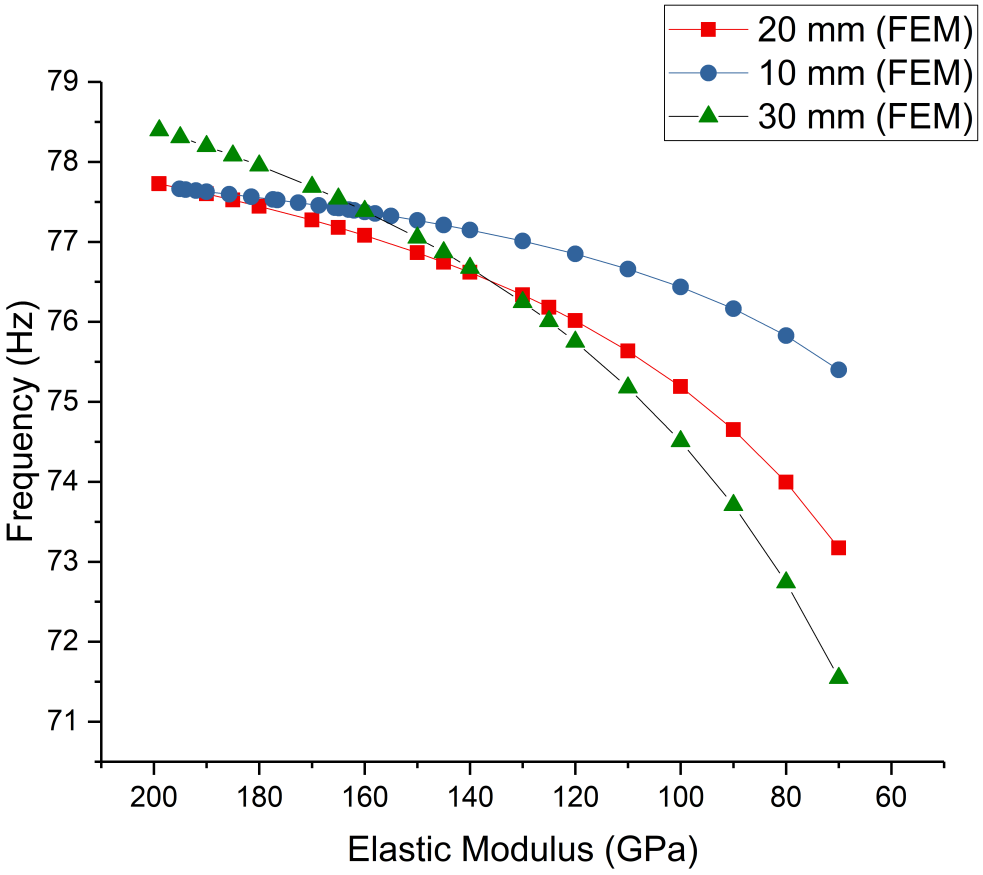

Figure 5.7: Finite Element Analysis of different flash lengths

5.2.3 Effect of Electric Field on Elastic Modulus

Elastic modulus was estimated for its corresponding flash condition by relating its respective frequency with FEA. Figure 5.8a shows the estimated elastic modulus as a function of temperature from the pyrometer. In this section, final results from sections 5.1 and 5.2, which are the baseline plot and damping coefficient as a function of temperature, were combined together to observe the effect of electric field or flash in 3Y-TZP. Figure 5.8 shows that the estimated elastic modulus of the sample during flash is lower than the baseline plot for every case. Also, note that this change in modulus differs for different flash lengths and this net change was found to reduce with increasing flash lengths. Figure 5.9 shows the damping coefficients for corresponding

current densities against the baseline values for different flash lengths. It was seen that damping coefficient for the same current density increases for flash lengths which could correspond to a lower modulus for higher current densities. This net change in values can seen in table 5.3

Current Density	**Pyrometer Temperature**	**Elastic Modulus (GPa)**	
($mA\ mm^{-2}$**)**	($^{\circ}C$)	**Baseline**	**Furnace Off (Flash On)**
10 mm flash length			
60	1030	141.337	96.606
80	1122	138.023	93.92
100	1202	136.791	86.655
120	1253	136.344	80.125
20 mm flash length			
60	1060	147.170	120.846
80	1120	145.454	113.003
100	1176	143.71	102.707
120	1237	141.819	92.719
30 mm flash length			
60	1061	143.595	128.985
80	1178	140.689	118.846
100	1264	137.806	106.6475
120	1335	135.804	97.352

Table 5.3: Elastic Modulus during flash

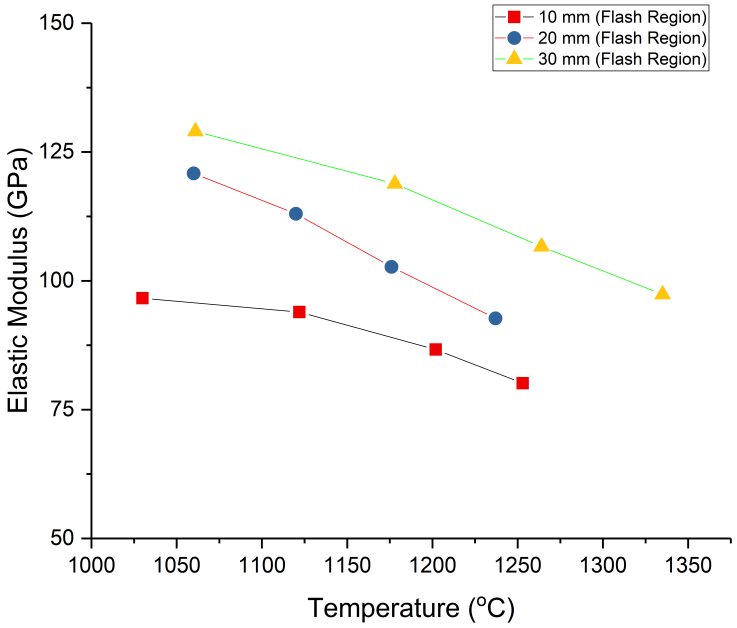

(a) Elastic Modulus vs Pyrometer temperature

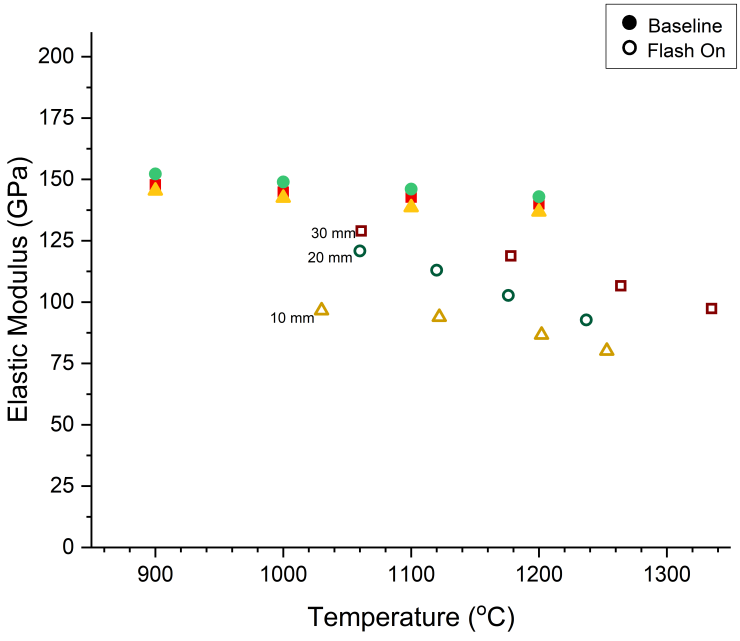

(b) Comparison of Elastic Modulus vs Temperature

Figure 5.8: Effect of Electric Field on Elastic Modulus

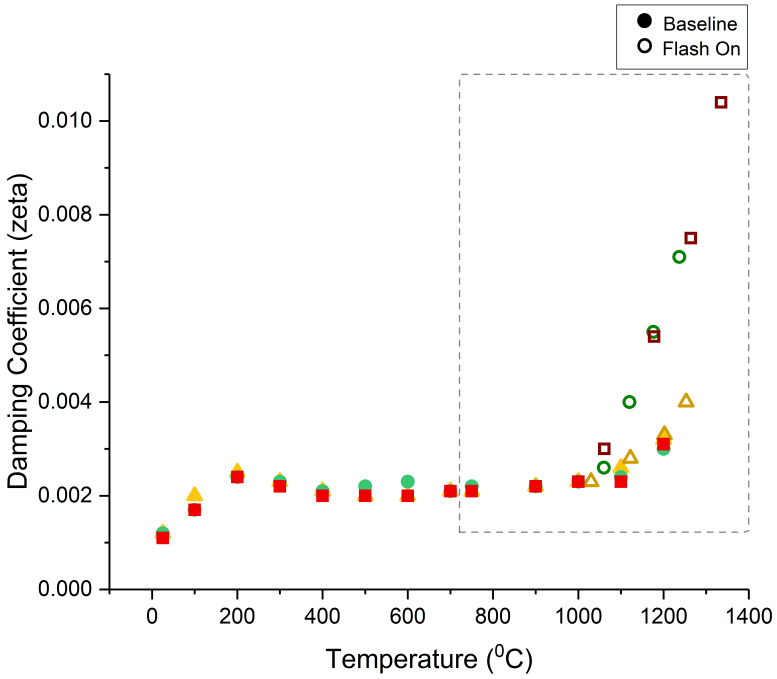

(a) Damping Coefficient vs Temperature

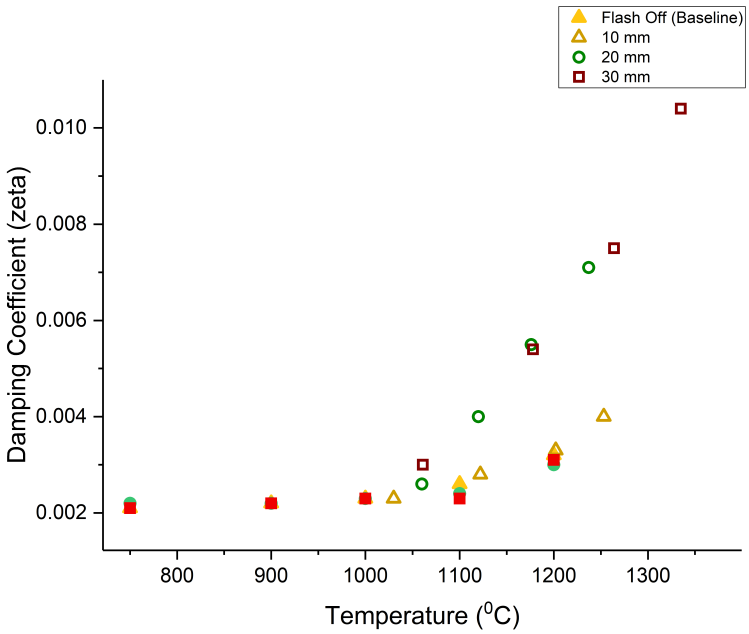

(b) Enlarged view of the black box from fig. 5.9a

Figure 5.9: Effect of Electric Field on the damping coefficient

5.2.4 Black Body Radiation model and Pyrometer

As mentioned in section 5.2.1, samples were flashed at different current densities and the voltage and current data was recorded into a computer using Matlab©. This data was then used to calculate the power and power density consumed per unit volume by the sample. Figure 5.10 shows the log plot of power density consumption over time for different flash lengths. On the left, the four visible plateaus for each flash length are the power densities measured for the previously mentioned current densities when the furnace was at $750°C$. When the furnace is turned off, the power consumption of the flashed region increases to maintain the sample temperature for a steady current flow. The plateaus on the right are for different current densities when the furnace was turned off . It is seen that power density consumed by the smallest flash length (10 mm) is the highest at about $700mWmm^{-3}$ for a current density of $120mAmm^{-2}$ and is lower for longer flash lengths.

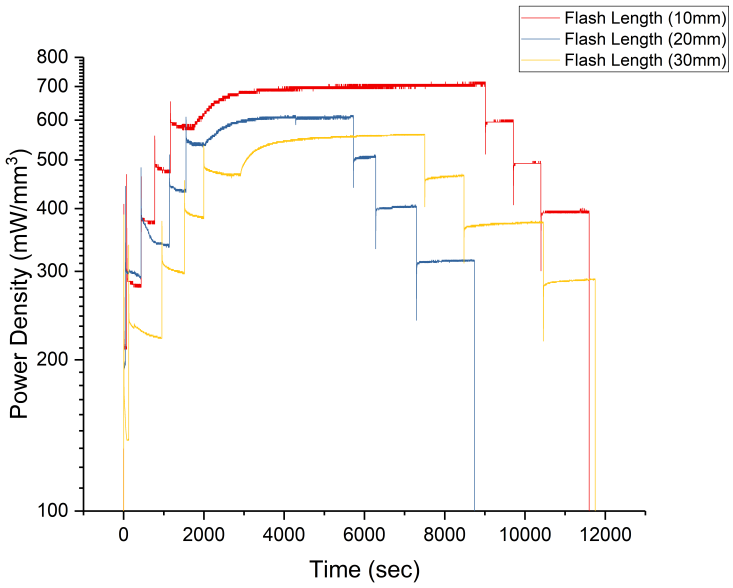

Figure 5.10: Power Density for different flash lengths

These power densities were then used to predict and measure the temperature of the flash

region by using the Black Body Radiation (BBR) model. BBR model uses the concept of joule heating to predict the temperature of the sample. Equation 5.1 is used to calculate the BBR temperature of the region undergoing flash. [27]

$$\frac{T}{T_0} = \left[1 + \frac{W_v}{\varepsilon\sigma T_0^4}\left(\frac{V}{A}\right)\right]^{1/4} , \tag{5.1}$$

where, T is the temperature of the flash region, T_0 is the furnace temperature, W_v is the power density, σ is the Stephen-Boltzmann constant ($5.6710^{-8}\ Wm^{-2}K^{-4}$, V is the volume, and A is the surface area of the flash region. Here, the emissivity of the sample was taken as 0.9 which has been measured by Terauds using Platinum standard [28]. These rods also had a constant VA ratio of 0.4575. When the BBR temperatures were compared to the pyrometer temperatures, it was observed that they were usually very close to each other with a maximum deviation of $96°C$.

Due to similar temperature estimations, plots shown in figures 5.8 remains pretty much the same with only a slight shift. The same goes for the damping coefficients measurements. The revised plots can be seen in figure 5.11. This further assert the reliability of both the temperature and modulus measurements obtained. Therefore, it is noted that there is significant change in elastic modulus for smaller flash lengths.

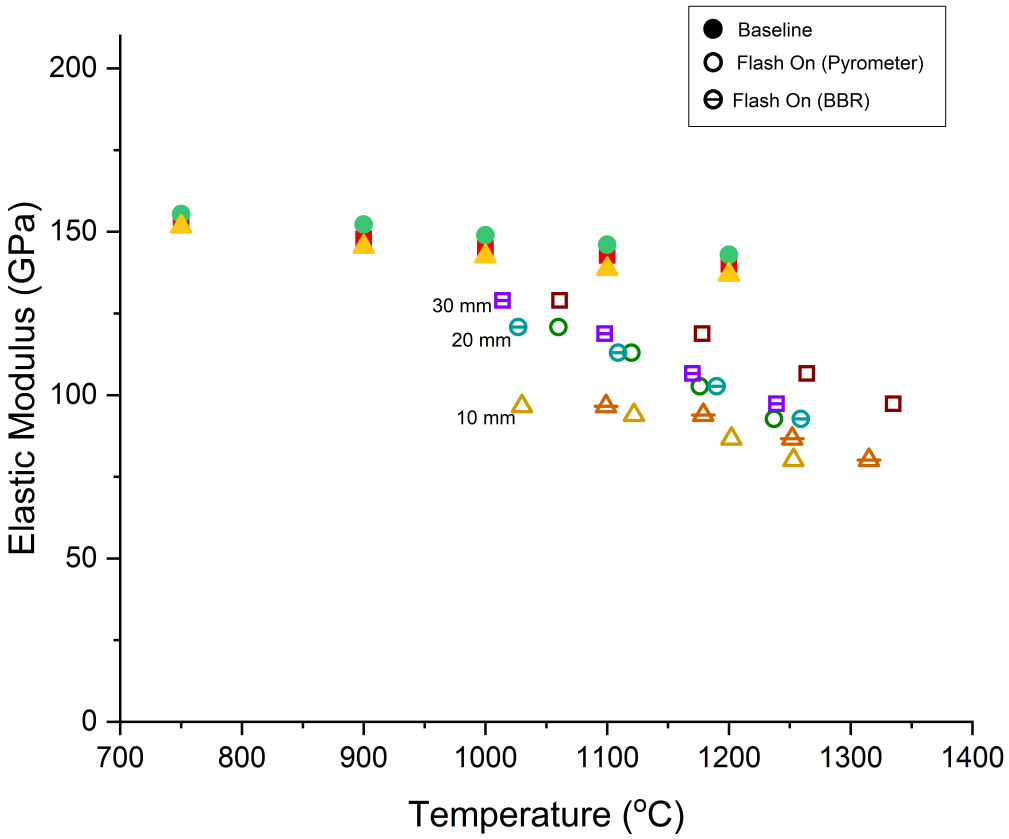

Figure 5.11: Comparison of the difference in BBR temperature and Pyrometer

Chapter 6

Discussion and Conclusion

6.1 Discussion

6.1.1 Sources of error in elastic modulus estimation

The results obtained in this study as displayed in chapter 5 show that there is considerable softening of or drop in elastic modulus during flash in an already dense 3Y-TZP coupled with an increase in damping coefficient. On revisiting the experimental setup and its procedure, there are a few factors that can have an affect on the outcome of the final results. These factors are:

- Improper bonding between the cement, rod and alumina tube.
- Platinum wires attached to the rod used for flash.
- Loose clamping of the sample on the sample holder.
- Placement of laser for recording vibrations.
- Effect of surrounding vibrations on the sample.

Of all the possible sources of error during the process, the error due to clamps and laser was easily eliminated by ensuring the tightness of clamp on sample and focusing the laser at the center of the sample. When motion was imparted to the sample by an impulse hammer, vibrations from the setup could couple with the vibrations of the sample resulting in visible noise in the FFT. This noise was reduced by adding a thick layer of Neoprene in all the joints in the setup,

thereby canceling surrounding vibrations giving a cleaner FFT. Improper bonding of cement between the tube and rod can sometimes result in a beats like behavior, where two waves with similar frequencies interfere to give a beats like pattern. This was easily identifiable by looking at the recoded signal in which case, an entire sample was remade from scratch.

The most important source of error that affected the vibrations was the wrapped platinum wire electrodes needed for flash. If the wrapping was not tight enough, a gap between the rod and wire would impede the free flowing motion leading to a beats like effect. When these wires were connected to the power supply, it was made sure that wires were loose enough to allow unimpeded motion but also tense enough, so that the wire would not rest on the furnace walls once the temperature is increased. However, When the same experiment was repeated without wires, it was noticed that the net change in frequency in both cases was quite close and was observed only at the beginning of the experiment. This difference was about 0.4 Hz. Furthermore, no change was found when the measurements were repeated after the furnace was cooled to room temperature bolstering the reliability of the frequency measurements.

Apart from the above mentioned experimental sources, what likely affects the elastic modulus estimations (not the frequency measurements) the most is the assumptions made while performing the finite element simulations. Here, two important assumptions were made: length of the cantilever beam; three distinct regions at uniform temperature. Length estimation was quite precise as confirmed by FEA at room temperature. But the assumption of only three distinct regions with separate elastic moduli is the major source of error. As mentioned before, it was assumed that there was no thermal/temperature gradient in the sample outside the furnace without the flash and adjacent to the flash region in case of flash. This might be valid for low temperature baseline measurement (up to $400°C$) as the effect is not that distinctive but at higher temperatures, due to higher convection rate and temperature gradient sample reaches higher temperatures even outside (adjacent regions) the furnace. Hence, forming a longer hot region

than assumed (but retaining the curve shape). This can also be seen in figure 5.6 as the estimation drifts away from the literature estimates. This makes sense because as the region becomes hotter, it softens resulting in the drop of frequency which can be seen in equation 4.1 and larger the region higher its effect on the frequency and hence, higher the drop. The same goes for the region close to the flash length. Hence, more temperature regions should be assumed for better simulations.

This would mean that the estimated elastic modulus during flash is a little higher bringing it closer to the baseline curve but also at the same time the baseline curve is expected to move up and by higher a amount because of a longer gradient. Regardless of which, there is distinctive softening during the flash and the net calculated difference in elastic modulus should hold up well.

6.1.2 Mechanism involved in flash sintering

This poses the next question, what is causing this higher softening and is this softening one of the primary reasons for flash sintering. The proposed mechanism should be able to explain the distinct characteristics of flash sintering which is: an abrupt non-linear rise in conductivity; rapid densification of the sample followed by the flash. Joule heating has been put forward as a possible explanation for flash sintering by a few researchers [29–31]. But this does not fall in place with temperatures measured during flash (platinum standards [32], BBR model and pyrometer measurements) and the temperature (very high) needed for sintering to occur at such high rates.

A mechanism was put forward by Raj, Francis, and Cologna [33] involves the generation of an avalanche of Frenkel defects in the lattice where non-linear lattice vibrations initiated during flash leads to the softening of lattice making it easier to create defects far above its thermal equilibrium concentration. Unusually high displacements of O and Ti in TiO_2 during the state of

flash confirm the hypothesis of non-linear vibrations at the onset of stage II of flash [34]. These PDF experiments were performed at Brookhaven National Laboratory (BNL). Also, Ti was quite well behaved but O atoms showed an erratic behavior (high disorder) to their movement asserting the occurence of non-linear vibrations.

Section 2.4 shows the dependence of activation energy on elastic modulus of material. High mean atomic displacements at BNL reflect an increase in bond length causing the potential well to shift up giving a lower modulus. Lower elastic modulus measured in this study also supports this result. Therefore for a softer material, activation energy for vacancy generation is lower and the same goes for interstitial formation as it is easier to compress the bonds to occupy an interstitial site. This has also been shown/predicted by Jongmanns [35] through Molecular Dynamics (MD) simulations of Aluminum single crystal. Three necessary conditions required in these simulations are: (i) the sample temperature should be above Debye Temperature, (ii) the phonons proliferate at a high rate, (iii) the phonon wavenumber or the lattice vibrations should be at the edge of the Brillouin zone. Since phonons were continuously added into the system, the kinetic energy increased to a certain extent after which it became stagnant. At this very instant, it was found that the excess energy was going in the creation of self-interstitials. Temperature at which these defect generation began was the Debye temperature of Aluminum which matches with flash conditions shown by Yadav [20]. Even if one of the conditions is not met, energy is dissipated from the system in the form of heat cooling the single crystal. Here, self-interstitials of 5 orders of magnitude higher than the thermal equilibrium concentration of vacant sites.

Further, high damping coefficients (zeta) measured in this study also support the theory of softening and defect generation. Higher zeta means higher internal friction implying that more external energy is converted into internal (potential) energy which could be a result of lattice imperfections/dislocations present in the material [36]. This existence of dislocations has also been found in TiO_2 where certain planes were more favored over others [37]. While the above

mentioned mechanism is still highly debated, these nonlinear lattice vibrations could in turn soften the shear modulus of the lattice and hence a lower elastic modulus which can be seen in the experiments performed in this thesis. Increase in damping coefficient could further support the idea of increased defect generation.

6.2 Conclusion and Future Experiments

Although, the flash phenomenon observed in flash sintering has just scratched the surface, it has an immense number of applications. Prospective applications are:

- Manufacturing tiles in large scales at a highly efficient rate.
- Recently, an aluminum alloy was flash sintered at room temperature from its powder [38]. This has a possibility to be extended to other materials, which are even conductive.
- Lower modulus during flash could help in easier shape forming of ceramics.
- Easier to cut through ceramics.
- Possible use in making small ceramic parts for medical devices, smartphone industry, artificial teeth and many more.
- Has scope of being used in additive manufacturing.
- Could be used a means to join broken ceramic parts.
- Making solid-state electrolytes for solid-state batteries and many more.

This highly energy efficient method has already been put to use by a few companies such as Lucideon for manufacturing tiles, Lupine labs and a few others.

Although the results from the experiments seem quite convincing, further experimentation needs to be done to fully understand the results. Some of the experiments which could be conducted are suggested below.

- Some decisive experiments for measuring the sample temperature during flash should be devised to assert the temperature estimates by BBR model and pyrometer.
- Eliminating the thermal gradient by having the sample as the same size as the furnace and a comparable flash length for a wider range of current densities. This could help to see why low current densities do not lead to full density.
- One of the most important experiments that could be done is the in-situ measurements during the current rate experiments. These experiments can tweaked as needed to see the subtle behavior of elastic modulus over a longer flash periods and wider current limits.
- The experiments performed and above suggested should be performed on different materials like materials which flash sinter, but also the materials which flash but do not sinter (during flash). This could help understand and differentiate the influence of field on materials.

Bibliography

[1] Randall M. German. Chapter one - introduction. In Randall M. German, editor, Sintering: from Empirical Observations to Scientific Principles, pages 1 – 12. Butterworth-Heinemann, Boston, 2014.

[2] Di Yang and H. Conrad. Influence of an electric field on the superplastic deformation of 3y-tzp. Scripta Materialia, 36(12):1431 – 1435, 1997.

[3] Suk-Joong L. Kang. 1 - sintering processes. In Suk-Joong L. Kang, editor, Sintering, pages 3 – 8. Butterworth-Heinemann, Oxford, 2005.

[4] R.M. German. 1 - thermodynamics of sintering. In Zhigang Zak Fang, editor, Sintering of Advanced Materials, Woodhead Publishing Series in Metals and Surface Engineering, pages 3 – 32. Woodhead Publishing, 2010.

[5] Suk-Joong L. Kang. 2 - thermodynamics of the interface2. In Suk-Joong L. Kang, editor, Sintering, pages 9 – 18. Butterworth-Heinemann, Oxford, 2005.

[6] F.B. Swinkels and M.F. Ashby. A second report on sintering diagrams. Acta Metallurgica, 29(2):259 – 281, 1981.

[7] Suk-Joong L. Kang. 4 - initial stage sintering. In Suk-Joong L. Kang, editor, Sintering, pages 39 – 55. Butterworth-Heinemann, Oxford, 2005.

[8] H.E. Exner and P. Bross. Material transport rate and stress distribution during grain boundary diffusion driven by surface tension. Acta Metallurgica, 27(6):1007 – 1012, 1979.

[9] B.H Alexander and R.W Balluffi. The mechanism of sintering of copper. Acta Metallurgica, 5(11):666 – 677, 1957.

[10] RISHI RAJ. Morphology and stability of the glass phase in glass ceramic systems. Journal of the American Ceramic Society, 64(5):245–248.

[11] Ricardo H. R. Castro. Overview of Conventional Sintering, pages 1–16. Springer Berlin Heidelberg, Berlin, Heidelberg, 2013.

[12] Suk-Joong L. Kang. 5 - intermediate and final stage sintering. In Suk-Joong L. Kang, editor, Sintering, pages 57 – 87. Butterworth-Heinemann, Oxford, 2005.

[13] Morteza Oghbaei and Omid Mirzaee. Microwave versus conventional sintering: A review of fundamentals, advantages and applications. Journal of Alloys and Compounds, 494(1):175 – 189, 2010.

[14] V G Karayannis. Microwave sintering of ceramic materials. IOP Conference Series: Materials Science and Engineering, 161(1):012068, 2016.

[15] Zhao-Hui Zhang, Zhen-Feng Liu, Ji-Fang Lu, Xiang-Bo Shen, Fu-Chi Wang, and Yan-Dong Wang. The sintering mechanism in spark plasma sintering fi?? proof of the occurrence of spark discharge. Scripta Materialia, 81:56 – 59, 2014.

[16] Dustin M. Hulbert, Andr Anders, Joakim Andersson, Enrique J. Lavernia, and Amiya K. Mukherjee. A discussion on the absence of plasma in spark plasma sintering. Scripta Materialia, 60(10):835 – 838, 2009.

[17] Cologna Marco, Rashkova Boriana, and Raj Rishi. Flash sintering of nanograin zirconia in ¡5 s at 850c. Journal of the American Ceramic Society, 93(11):3556–3559.

[18] Marco Cologna, John S.C. Francis, and Rishi Raj. Field assisted and flash sintering of alumina and its relationship to conductivity and mgo-doping. Journal of the European Ceramic Society, 31(15):2827 – 2837, 2011.

[19] Shikhar K. JHA, Kalvis TERAUDS, Jean-Marie LEBRUN, and Rishi RAJ. Beyond flash sintering in 3 mol Journal of the Ceramic Society of Japan, 124(4):283–288, 2016.

[20] Devinder Yadav and Rishi Raj. Two unique measurements related to flash experiments with yttriafiQustabilized zirconia. Journal of the American Ceramic Society, 100(12):5374–5378, 12 2017.

[21] Jean-Marie LEBRUN Punith Kumar M K, Devinder Yadav and Rishi RAJ. Flash sintering with current-rate: A different approach. Journal of American Ceramic Society, Under review.

[22] Bola Yoon, Devinder Yadav, Sanjit Ghose, and Rishi Raj. Reactive flash sintering: Mgo and fiQual2o3 transform and sinter into singlefiQuphase polycrystals of mgal2o4. Journal of the American Ceramic Society, 8 2018.

[23] Jr. Callister, William D. and David G. Rethwisch. Atomic Structure and Interatomic Bonding, pages 18–43. John Wiley & SOns, Inc., Hoboken, NJ, 2009.

[24] F. Frster and W. Kster. Modulus of elasticity and damping in relation to the state of the material. Journal of the Institution of Electrical Engineers, 84(509):558–564, May 1939.

[25] Masahiko Shimada, Ken'ichi Matsushita, Shusei Kuratani, Taira Okamoto, Mjtsue Koizumi, Koji Tsukuma, and Takaaki Tsukidate. Temperature dependence of young's modulus and internal friction in alumina, silicon nitride, and partially stabilized zirconia ceramics. Journal of the American Ceramic Society, 67(2):CfiQu23–CfiQu24.

[26] Jane W. Adams, Robert Ruh, and K. S. Mazdiyasni. Young's modulus, flexural strength, and fracture of yttria-stabilized zirconia versus temperature. Journal of the American Ceramic Society, 80(4):903–908.

[27] Rishi Raj. Joule heating during flash-sintering. Journal of the European Ceramic Society, 32(10):2293 – 2301, 2012.

[28] Kalvis Terauds, Jean-Marie Lebrun, Hyun-Hwi Lee, Tae-Yeol Jeon, Sang-Hyeon Lee, Jung Ho Je, and Rishi Raj. Electroluminescence and the measurement of temperature during stage iii of flash sintering experiments. Journal of the European Ceramic Society, 35(11):3195 – 3199, 2015.

[29] Salvatore GRASSO, Yoshio SAKKA, Nicolas RENDTORFF, Chunfeng HU, Giovanni MAIZZA, Hanna BORODIANSKA, and Oleg VASYLKIV. Modeling of the temperature distribution of flash sintered zirconia. Journal of the Ceramic Society of Japan, 119(1386):144–146, 2011.

[30] Raschid Baraki, Sebastian Schwarz, and Olivier Guillon. Effect of electrical field/current on sintering of fully stabilized zirconia. Journal of the American Ceramic Society, 95(1):75–78, 1 2012.

[31] Jungdeok Park and IfiQuWei Chen. In situ thermometry measuring temperature flashes exceeding 1,700c in 8molJournal of the American Ceramic Society, 96(3):697–700, 3 2013.

[32] J.-M. Lebrun, C. S. Hellberg, S. K. Jha, W. M. Kriven, A. Steveson, K. C. Seymour, N. Bernstein, S. C. Erwin, and R. Raj. In-situ measurements of lattice expansion related to defect generation during flash sintering. Journal of the American Ceramic Society, 100(11):4965–4970.

[33] John S.C. Francis, Marco Cologna, and Rishi Raj. Particle size effects in flash sintering. Journal of the European Ceramic Society, 32(12):3129 – 3136, 2012.

[34] Bola Yoon, Devinder Yadav, Rishi Raj, Emanuele Sortino, Sanjit Ghose, Pankaj Sarin, and Daniel Shoemaker. Measurement of o and ti atom displacements in tio2 during flash sintering experiments. Journal of the American Ceramic Society, 101(5):1811–1817.

[35] M Jongmanns, R Raj, and D E Wolf. Generation of frenkel defects above the debye temperature by proliferation of phonons near the brillouin zone edge. New Journal of Physics, 20(9):093013, 2018.

[36] Clarence Zener. Internal friction in solids. Proceedings of the Physical Society, 52(1):152, 1940.

[37] S.K. Jha, J.M. Lebrun, K.C. Seymour, W.M. Kriven, and R. Raj. Electric field induced texture in titania during experiments related to flash sintering. Journal of the European Ceramic Society, 36(1):257 – 261, 2016.

[38] Brandon McWilliams, Jian Yu, and Frank Kellogg. Sintering aluminum alloy powder using direct current electric fields at room temperature in seconds. Journal of Materials Science, 53(12):9297–9304, Jun 2018.